Adiabatic rf Pulses: Applications to *In Vivo* NMR

ROBIN A. DE GRAAF and KLAAS NICOLAY

Department of in vivo NMR, Bijvoet Center, Utrecht University, The Netherlands

ABSTRACT: Adiabatic pulses are amplitude- and frequency-modulated pulses that are insensitive to the effects of $\mathbf{B}_1$-inhomogeneity and frequency offset. From the classical adiabatic passage experiments, the adiabatic condition is derived and analyzed. From the adiabatic condition, amplitude and frequency modulation functions are derived and optimized over predetermined radio frequency amplitude and frequency offset ranges. Description of the selective inversion and refocusing properties of adiabatic full-passage pulses leads to the principle of plane rotation pulses, of which the BIR-4 ($\mathbf{B}_1$-insensitive rotation) pulse will be discussed in detail. Theoretical simulations based on the Bloch equations, three-dimensional vector diagrams, and experimental applications demonstrate the utility and performance of the adiabatic pulses for *in vivo* NMR and for liquid state high-resolution NMR. Concepts Magn Reson **9:** 247–268, 1997

KEY WORDS: adiabatic pulses, adiabatic condition, amplitude and frequency modulation, $\mathbf{B}_1$-insensitive rotation, frequency offset, frequency selection, plane rotation, rf inhomogeneity

INTRODUCTION

The transition energies between various energy states encountered in NMR are extremely small compared with normal thermal energies, so the energy states are almost equally populated, which leads to a small net energy absorption when an NMR experiment is performed. This makes NMR an intrinsically nondestructive and noninvasive technique, ideally suited for studying the metabolism and anatomical structure of intact biological systems. However, the almost equally populated energy states also make NMR an insensitive technique. Moreover, given the fact that metabolites *in vivo* are present only in the millimolar range (or lower), it needs no further explanation that optimized signal detection in an *in vivo* NMR experiment is critical, especially with low-sensitivity nuclei such as ^{13}C and ^{31}P.

Conventional NMR radio frequency (rf) coils, such as solenoidal and saddle-shaped coils, are not optimal in this respect, because of their large size relative to the volume of interest (VOI) under investigation. Surface coils, on the other hand, can be relatively small and can be placed adjacent to a larger object. Therefore, the surface coil receiver can obtain a higher signal-to-noise ratio (S/N) from a restricted area than can any other NMR rf coil. Other useful characteristics of surface coils are that they provide a degree of spatial localization and that their geometry and size can be designed to suit the shape of the object and the VOI.

Received 18 September 1996; revised 6 February 1997; accepted 7 February 1997.

Correspondence to: Robin A. de Graaf, Department of *in vivo* NMR, Bijvoet Center for Biomolecular Research, Utrecht University, Bolognalaan 50, 3584 CJ Utrecht, The Netherlands. Phone: +30 2535515; Fax: +30 2535561; E-mail: degraaf@bijvoet.ruu.nl.

 CCC 1043-7347/97/040247-22

Surface coils and conventional coils differ greatly in the rf fields they generate. Conventional coils generate, in principle, a homogeneous rf field; the field strength $\mathbf{B}_1$ is constant over the region in which the sample is placed. Surface coils, on the other hand, produce a highly inhomogeneous rf field, in which $\mathbf{B}_1$ decreases with distance from the coil. Figure 1 shows the sensitivity profiles in the *xy* plane ($z = 0$) perpendicular to the direction of the main magnetic field $\mathbf{B}_0$ for a 2.0 cm diameter, circular, single-turn surface coil lying in the *xz* plane (*y* denotes the axial distance from the coil). The sensitivity is proportional to $\mathbf{B}_1(\mathbf{r})\sin(\theta(\mathbf{r}))$, where $\mathbf{B}_1(\mathbf{r})$ is the rf field strength, and $\theta(\mathbf{r})$ is the flip angle at position $\mathbf{r}$ from the coil. Figure 1(A) shows the sensitivity profile when the flip angle is independent of $\mathbf{r}$ (uniform excitation with a $\mathbf{B}_1$-insensitive, adiabatic rf pulse). In this case, the sensitivity is proportional to $\mathbf{B}_1(\mathbf{r})$, the spatially dependent rf field strength. Close to the coil, the $\mathbf{B}_1$ magnitude (and, through the reciprocity principle (*1*) also the sensitivity) is very high and decreases smoothly with increasing distance from the coil. To a first approximation [*2*], the sensitive volume of a circular surface coil can be described as a hemisphere of 1 coil radius.

The inhomogeneous rf field has major implications when the surface coil is used not only for signal reception but for rf pulse transmission as well. The flip angle generated by a conventional (square) rf pulse is given by

$$\theta(\mathbf{r}) = 2\pi\gamma\mathbf{B}_1(\mathbf{r})T_p \qquad [1]$$

$\theta(\mathbf{r})$ is the flip angle (in radians), $\gamma\mathbf{B}_1(\mathbf{r})$ is the rf field strength (in Hertz) at position $\mathbf{r}$, and T_p is the pulse duration (in seconds).

Figure 1(B) shows the sensitivity profile when the surface coil is used for transmitting a conventional square 90° rf pulse. The rf pulse was calibrated to give a 90° flip angle at the coil center (spin–echo sequence with repetition time T_R, 2000 ms; echo time T_E, 75 ms; and $\mathbf{B}_1$-insensitive, adiabatic, slice-selective refocusing pulses (*3*, *4*)). In this experiment, the volume that contributes the signal is significantly reduced, when compared with the situation where the flip angle is $\mathbf{B}_1$-independent (Fig. 1(A)), and the profile close to the coil oscillates and even becomes zero and negative (not visible) because of larger flip angles (e.g., $\mathbf{B}_1(\mathbf{r})\sin(270°) = -\mathbf{B}_1(\mathbf{r})$). For more sophisticated experiments, such as multiple-quantum coherence filtering (*5*, *6*), consisting of three 90° and three 180° rf pulses, the signal received will be restricted to an even smaller region, as shown in Fig. 1(C).

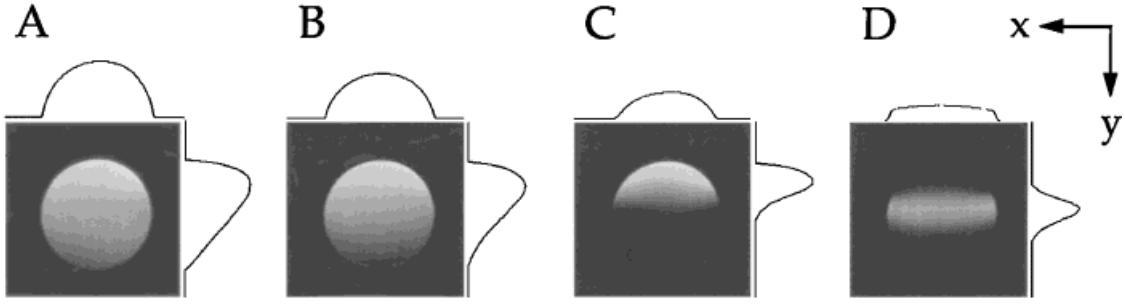

Figure 1 ^{1}H NMR images obtained with a 2.0 cm diameter surface coil of a 1.5 cm diameter sphere containing water when using (A) $\mathbf{B}_1$-independent (adiabatic) and (B)–(D) $\mathbf{B}_1$-dependent excitation. In (A) an AHP pulse achieves uniform excitation irrespective of the $\mathbf{B}_1$ magnitude. The profiles on the top and to the right of the images represent the total integrated signal in that specific direction. For (A) this profile is simply determined by the $\mathbf{B}_1$ profile of the surface coil (the $\mathbf{B}_1$ field strength is high close to the coil and decreases with distance from the coil) and the sample dimensions. In (B) and (C) excitation is accomplished with a square 90° rf pulse and a gradient-enhanced MQC (geMQC) filtering sequence consisting of six square rf pulses, respectively, calibrated to give the correct flip angle (90° or 180°) at the coil center. In (D) the square rf pulses of the geMQC sequence were calibrated on the spectral water signal. The profiles of (B), (C), and (D) no longer represent the $\mathbf{B}_1$ profile of the coil but also are modulated by the $\mathbf{B}_1$-dependent flip angle, consequently leading to signal loss. The integrated intensities of the profiles shown in (B), (C), and (D) are 79%, 34%, and 24%, respectively, of that shown in (A).

It must be noted that Figs. 1(B) and 1(C) show the most favorable, but not the most realistic, cases. Normally, the flip angle would be calibrated on the spectral water signal (and not on the image readout profiles), so the optimal pulse length would not give a 90° flip angle at the coil center but farther away from the coil. Figure 1(D) shows the sensitivity profile of the multiple-quantum coherence (MQC) filtering sequence when the flip angle is calibrated on the spectral water signal. The profile is shifted farther away from the surface coil, leading to more signal loss.

Although undesirable in most experiments, the $\mathbf{B}_1$-dependence of conventional rf pulses can, in some cases, be used to advantage. When rf pulses with correctly calibrated flip angles are used, the $\mathbf{B}_1$-dependence can be used for a crude spatial localization, as shown in Fig. 1(D). This is essentially the basis of spatial localization with depth pulses (*7*, *8*).

It can be concluded from Fig. 1 that, in most experiments, signal is forfeited and S/N is decreased when a surface coil is used for the transmission of conventional (square) rf pulses. This problem can be solved by using a circumscribing volume coil for (relatively) homogeneous pulse transmission and a surface coil for signal reception. However, incomplete elimination of residual inductive coupling between the coils can cause distortions in the rf field and, consequently, signal loss. Signal loss with this experimental setup also will occur because each coil produces a different $\mathbf{B}_1$ flux, causing the phases of transmission and reception to be mismatched as a function of position. This leads to phase cancellation of signal (*9*).

Alternatively, rf pulses that operate according to adiabatic principles (*3, 4, 6, 10–16*) can be used. Adiabatic pulses generate a uniform flip angle despite variations in $\mathbf{B}_1$, provided that the $\mathbf{B}_1$ field is above a threshold. In this way, surface coil NMR experiments can be executed conveniently in a single-coil mode, in which the high sensitivity of surface coil reception and a constant phase relation between transmission and reception are maintained. Another practical advantage of adiabatic pulses is that they eliminate the time-consuming calibrations of rf power (or pulse length) required for conventional pulses. Adiabatic pulses require only a one-time experimental determination of the minimum threshold $\mathbf{B}_1$ at which the pulses become operational with a particular rf coil. Using a slightly larger $\mathbf{B}_1$ than the determined minimum threshold eliminates the need for $\mathbf{B}_1$ calibration in subsequent experiments.

This article reviews the fundamental principles of adiabatic pulses, starting with pulses based on the classical adiabatic half-passage (AHP) and adiabatic full-passage (AFP) experiments, which induce spin excitation and inversion, respectively. However, these two pulses have limited use; they cannot induce *plane* rotations (they cannot rotate the magnetization about any arbitrary axis), which, for example, are needed in spin–echo and polarization transfer experiments. The development of adiabatic plane rotation pulses has greatly broadened the applications of these pulses. The variable flip angle pulse BIR-4 ($\mathbf{B}_1$-insensitive rotation, four-segment pulse) (*13*) is the most versatile adiabatic-plane rotation pulse. The principles of BIR-4 are discussed later in detail.

ADIABATIC PRINCIPLES

Rotation Frames

The general principles of adiabatic pulses are best illustrated with a single set of spins with Larmor frequency ω_0. The motion of spins induced by an adiabatic pulse can be visualized best in a reference frame $x'y'z'$ that rotates about z' (which is collinear with the main magnetic field $\mathbf{B}_0$) at the instantaneous frequency $\omega(t)$ of the pulse. This reference frame is here called the frequency frame. In the frequency frame $\mathbf{B}_1(t)$ does not precess in the transverse plane: $\mathbf{B}_1(t)$ has a constant orientation (arbitrarily chosen along x', Fig. 2(A)). Because adiabatic pulses are amplitude- and frequency (or phase) modulated pulses, the frequency of the pulse $\omega(t)$ deviates from the Larmor frequency as a function of time. Consequently, the spins will encounter an additional magnetic field along z' of magnitude $(\Delta\omega(t)/\gamma)$, where $\Delta\omega(t)$ is defined as $(\omega(t) - \omega_0)$ and γ is the magnetogyric ratio. Therefore, the magnitude of the effective magnetic field $\mathbf{B}_e(t)$ in the frequency frame becomes

$$B_e(t) = |\mathbf{B}_e(t)| = \sqrt{B_1^2(t) + (\Delta\omega(t)/\gamma)^2} \quad [2]$$

In all adiabatic transformations, the orientation and the magnitude of the time-dependent $\mathbf{B}_e(t)$ vector is modulated. The motion of spins in the presence of an adiabatic pulse can be divided in two categories: (spin) components that are

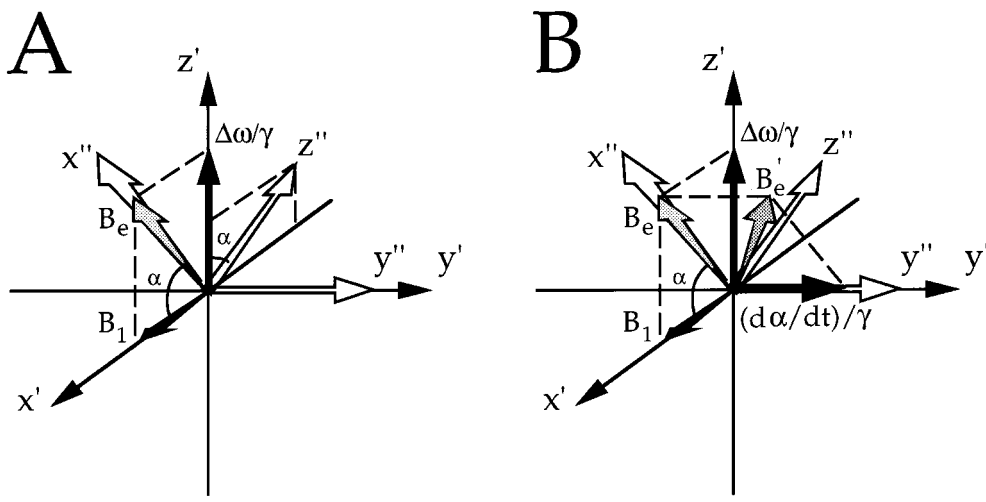

Figure 2 The relation between magnetic field vectors in rotating frames used to describe adiabatic pulses. (A) The frequency frame $x'y'z'$ precesses at the instantaneous frequency of the rf pulse, making the $\mathbf{B}_1$ orientation, abitrarily chosen along x', static. (B) The second rotating frame $x''y''z''$ rotates about y' with angular velocity $(d\alpha/dt)$ of the $\mathbf{B}_e$ rotation in the frequency frame. In the second rotating frame, the $\mathbf{B}_e$ orientation is static, leading to an additional vector $((d\alpha/dt)/\gamma)$ along y'' as $\mathbf{B}_e$ is rotating.

collinear with or perpendicular to $\mathbf{B}_e(t)$ at the onset of the pulse. Both types of motion can be described best in a second rotating frame $x''y''z''$ (Fig. 2(A)). In the second rotating frame, the orientation of $\mathbf{B}_e(t)$ is constant (except for discontinuous inversions, as for the BIR-4 plane rotation pulse). The second rotating frame changes its orientation with $\mathbf{B}_e(t)$ at the instantaneous angular velocity of $(d\alpha(t)/dt)$, relative to the frequency frame. $\alpha(t)$ is given by

$$\alpha(t) = \arctan\left(\frac{\Delta\omega(t)}{\gamma B_1(t)}\right) \qquad [3]$$

In the second rotating frame $x''y''z''$, there is an additional contribution to the effective field along the y'' axis of magnitude $((d\alpha(t)/dt)/\gamma)$, by analogy with the existence of $(\Delta\omega(t)/\gamma)$ in the frequency frame $x'y'z'$. The effective field in the second rotating frame, $\mathbf{B}'_e(t)$, becomes the vector sum of $\mathbf{B}_e(t)$ and $((d\alpha(t)/dt)/\gamma)[\boldsymbol{y}'']$, where $[\boldsymbol{y}'']$ is a unit vector along y'' (Fig. 2(B)). The magnitude of the effective magnetic field in the second rotating frame is given by

$$B'_e(t) = \sqrt{\left(B_e^2(t) + ((d\alpha(t)/dt)/\gamma)^2\right)} \qquad [4]$$

Provided that

$$|(d\alpha(t)/dt)/\gamma| \ll |\mathbf{B}_e(t)| \quad \text{or } |\gamma B_e(t)(d\alpha(t)/dt)^{-1}| \gg 1 \qquad [5]$$

This is known as the adiabatic condition, $\mathbf{B}'_e(t) \approx \mathbf{B}_e(t)$. When the adiabatic condition is satisfied, magnetization vectors that initially are collinear with $\mathbf{B}_e(t)$ will stay that way during the pulse when $\mathbf{B}_e(t)$ changes with time. Magnetization vectors that are perpendicular to $\mathbf{B}_e(t)$ at the onset of the pulse will remain in the plane perpendicular to $\mathbf{B}_e(t)$ and will rotate in the second rotating frame $x''y''z''$ about $\mathbf{B}_e(t)$, through an angle $\beta(t)$ given by Eq. [6]:

$$\beta(t) = \gamma\int_0^t \mathbf{B}_e(t')dt' = \gamma\int_0^t \sqrt{\left(B_1^2(t') + (\Delta\omega(t')/\gamma)^2\right)}\,dt' \qquad [6]$$

Because of $\mathbf{B}_1$ inhomogeneities, $\beta(t)$ will be a function of position.

Adiabatic Half- and Full-Passage Pulses

Adiabatic pulses are characterized by specific rf amplitude $\mathbf{B}_1(t)$ and frequency $\boldsymbol{\Delta\omega}(t)$ modulation functions. The magnetic field vectors encountered

in the frequency frame can be written as follows:

$$\mathbf{B}_1(t) = \mathrm{B}_{1\,\max} f_B(t)[\boldsymbol{x}'] \qquad [7]$$

$$\left(\frac{\boldsymbol{\Delta\omega}(t)}{\gamma}\right) = \left(\frac{\Delta\omega_{\max}}{\gamma}\right) f_\omega(t)[z'] \qquad [8]$$

where $f_B(t)$ and $f_\omega(t)$ are unitless, normalized modulation functions; $\mathrm{B}_{1\,\max}$ and $\Delta\omega_{\max}$ are the modulation amplitudes of $\mathbf{B}_1(t)$ and $\boldsymbol{\Delta\omega}$(t), and $[\boldsymbol{x}']$ and $[z']$ are unit vectors that identify the x' and y' axes of the frequency frame, respectively. Figures 3(A) and 3(B) show the $\mathbf{B}_1(t)$ and $\boldsymbol{\Delta\omega}(t)$ modulations for $f_B(t) = \mathrm{sech}[\beta((2t/T) - 1)]$ and $f_\omega(t) = \tanh[\beta(1 - (2t/T))]$, with t varying from 0 to T and β defining the cutoff points for the infinite sech and tanh functions. β is typically chosen as $\mathrm{sech}\beta = 0.01$ (1% cutoff level). This pair of modulation functions defines the well-known Silver-Hoult hyperbolic secant pulse (*10*). Adiabatic pulses can be implemented with amplitude and phase modulation, and the time-dependent $\mathbf{B}_1$ phase $\phi(t)$ is given by Eq. [9]:

$$\phi(t) = \int_0^t \Delta\omega(t')\,\mathrm{d}t' \qquad [9]$$

The $\phi(t)$ modulation of the hyperbolic secant pulse is shown in Fig. 3(C).

Alternatively, as is often done in the earlier literature on adiabatic pulses, the $\mathbf{B}_1(t)$ and $\boldsymbol{\Delta\omega}(t)$ modulations can be visualized in a frame *xyz* rotating with a constant frequency about z (which is collinear with the main magnetic field $\mathbf{B}_0$), at, for instance, the Larmor frequency ω_0 of the

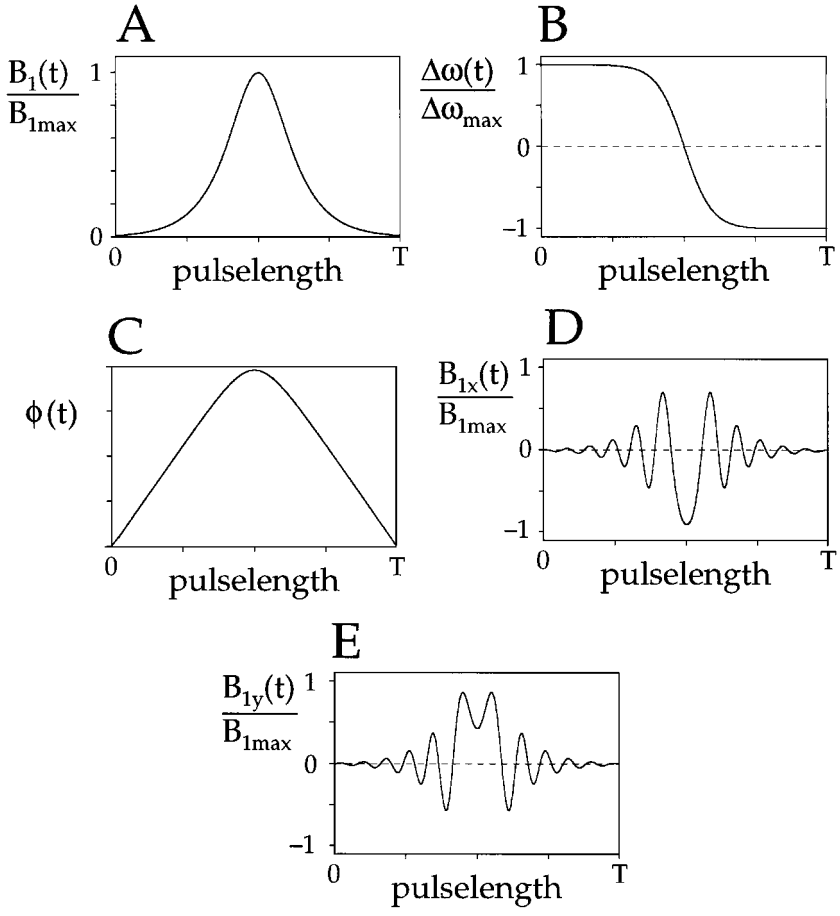

Figure 3 (A) rf amplitude $\mathbf{B}_1(t)$ and (B) frequency $\boldsymbol{\Delta\omega}(t)$ modulation functions of a hyperbolic secant pulse. (C) Phase $\phi(t)$ modulation can be used instead of frequency modulation by calculating the time integral of the frequency modulation. The maximum phase modulation was set to 2000°. To describe the rf pulse in the laboratory frame, real and imaginary rf amplitudes, (D) $\mathbf{B}_{1x}(t)$ and (E) $\mathbf{B}_{1y}(t)$ can be used.

spins. $\mathbf{B}_1(t)$ can be described as a time-dependent complex number:

$$\begin{aligned}\mathbf{B}_1(t) &= \mathrm{B}_{1\,\max} f_B(t) e^{i\Delta\omega_{\max}\int_0^t f_\omega(t')\mathrm{d}t'} \\ &= \mathrm{B}_{1\,\max} f_B(t) e^{i\phi(t)} \\ &= \mathrm{B}_{1\,\max} f_B(t)[\cos\phi(t)[\boldsymbol{x}] + i\sin\phi(t)[\boldsymbol{y}]] \\ &= \mathrm{B}_{1x}(t)[\boldsymbol{x}] + i\mathrm{B}_{1y}(t)[\boldsymbol{y}] \qquad [10]\end{aligned}$$

The real and imaginary parts of $\mathbf{B}_1(t)$ in this rotating frame, $\mathbf{B}_{1x}(t)$ and $\mathbf{B}_{1y}(t)$, are along x and y, respectively. These modulations are shown in Figs. 3(D) and 3(E). Although used in some (earlier) papers about adiabatic pulses (*3*, *10*), this representation does not give any insight about the principles of adiabatic pulses, and therefore the formalism for the $\mathbf{B}_1(t)$ and $\boldsymbol{\Delta\omega}(t)$ modulations given by Eqs. [7] and [8] is preferred and will be used here.

All adiabatic pulses are derived from the classical adiabatic passage experiment, which originates from continuous-wave NMR. In this experiment, the rf frequency $\omega(t)$ is varied at a constant rate from $+(\Delta\omega_{\max}/\gamma)$ to $-(\Delta\omega_{\max}/\gamma)$; that is $f_\omega(t) = 1 - (2t/T)$. $\mathbf{B}_1(t)$ remains constant ($f_B(t) = 1$). At the onset of the experiment, $\boldsymbol{\omega}(t)$ deviates substantially from the spin Larmor frequency ω_0, so that $|\Delta\omega(0)/\gamma)| \gg \mathbf{B}_1$ and therefore $\mathbf{B}_e(0) \approx \Delta\omega_{\max}/\gamma[z']$. $\mathbf{M}$, initially collinear with $\mathbf{B}_e(t)$, will remain so throughout the rf pulse, provided that the adiabatic condition is satisfied. Because $\mathbf{B}_e(t)$ rotates from $+z'$ to $-z'$ in the classical adiabatic passage experiment, $\mathbf{M}$ will be inverted (called AFP). In the case of an AHP pulse, $\mathbf{B}_e(t)$ rotates by only 90° from $+z'$ to $+x'$, and $\mathbf{M}$ will be excited onto the transverse plane.

Figure 4 shows the on-resonance rotations of magnetization vectors $\boldsymbol{M}_x$ and $\boldsymbol{M}_y$, initially perpendicular to $\mathbf{B}_e$ and $\boldsymbol{M}_z$ parallel to $\mathbf{B}_e$. The $f_B(t)$ and $f_\omega(t)$ modulation functions are not specified, but they satisfy the adiabatic condition during the entire pulse. Furthermore, $\mathbf{B}_1 = 0$ and $(\boldsymbol{\Delta\omega}/\gamma) = (\omega_{\max}/\gamma)\,[z'] = \mathbf{B}_e$ at the beginning of the pulse, $\mathbf{B}_1 = \mathbf{B}_{1\,\max}[\boldsymbol{x}'] = \mathbf{B}_e$ and $(\boldsymbol{\Delta\omega}/\gamma) = 0$ in the middle, and $\mathbf{B}_1 = 0$ and $(\boldsymbol{\Delta\omega}/\gamma) = -(\omega_{\max}/\gamma)[\boldsymbol{z}'] = \mathbf{B}_e$ at the end (Fig. 3).

From Fig. 4 it can be seen that because the $\mathbf{B}_1$ magnitude merely determines the rate at which $\mathbf{B}_e$ rotates the inversion of $\boldsymbol{M}_z$ from $+z'$ to $-z'$ is relatively insensitive to the $\mathbf{B}_1$ magnitude, and, as long as the rate of change of $\mathbf{B}_e$ (i.e., $(\mathrm{d}\alpha(t)/\mathrm{d}(t))$ is much smaller than its magnitude (when the adiabatic condition, Eq. [5], is satisfied), $\boldsymbol{M}_z$ will remain along $\mathbf{B}_e$. Another feature that can be deduced from Fig. 4 is that AHP or AFP pulses can execute only well-defined excitation (i.e., $\boldsymbol{M}_z \rightarrow \boldsymbol{M}_{xy}$ or inversion ($\boldsymbol{M}_z \rightarrow -\boldsymbol{M}_z$) transformations. For these transformations a unique rotation axis, y', exists, and the transformation induced is either a 90° or 180° rotation about this axis. When $\mathbf{M}$ has components that are parallel and perpendicular to $\mathbf{B}_e$ at the onset of the rf pulse, the

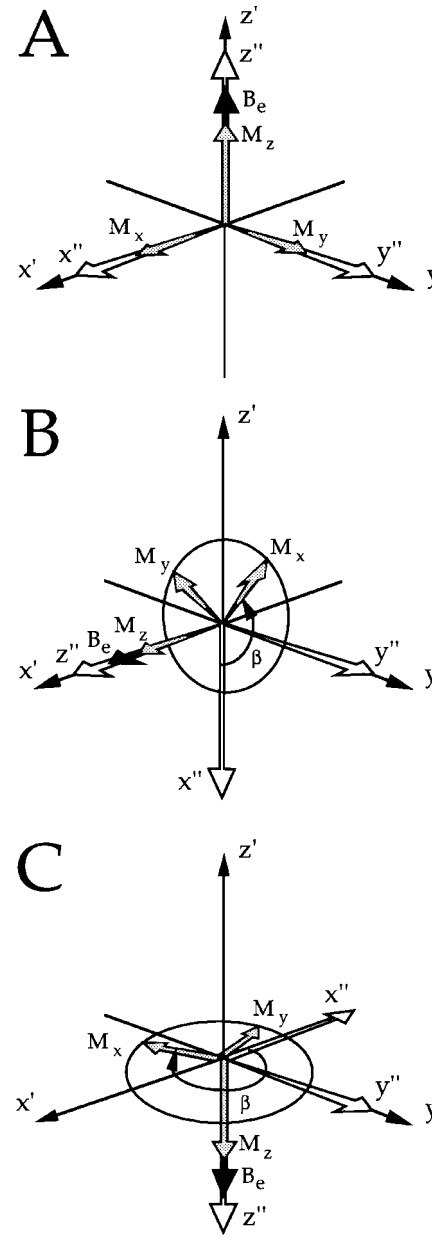

Figure 4 On-resonance rotations of the effective field $\mathbf{B}_e$ during an AFP pulse. Vector representations show (A) the onset of the pulse, (B) halfway through the pulse, and (C) the end of the pulse.

rotations induced by AHP and AFP pulses can no longer be described by a single rotation axis. The component of **M** parallel to $\mathbf{B}_e$ at the onset of the rf pulse (M_z in Fig. 4) will rotate by 90° or 180° about y', as described above. Components of **M** that are perpendicular to $\mathbf{B}_e$ at the onset of the rf pulse (M_x and M_y in Fig. 4) will rotate about $\mathbf{B}_e$ through an angle β given by Eq. [6], which depends on the distance from the coil as well as on the $\mathbf{B}_1(t)$ and $(\Delta\boldsymbol{\omega}(t)/\gamma)$ modulations used. By contrast, the aforementioned inversion and excitation transformations are relatively $\mathbf{B}_1$ insensitive and can be achieved with a wide range of pulse modulation functions.

Pulses that are based on adiabatic passage principles induce only the transformations $(0, 0, M_z) \rightarrow (M_x, 0, 0)$ (spin excitation by adiabatic half passage) or $(0, 0, M_z) \rightarrow (0, 0, -M_z)$ (spin inversion by adiabatic full passage). In general, these pulses cannot induce plane rotations, because a plane rotation pulse rotates all magnetization vectors with arbitrary orientations about a single rotation axis through the same angle. Such rotations are required in many NMR experiments. For example, plane rotations that induce the transformation $(\mathbf{M}_x, \mathbf{M}_y, \mathbf{M}_z) \rightarrow (M_x, -M_z, M_y)$ (90° plane rotation) are required in stimulated-echo and polarization transfer experiments; rotations such as $(M_x, M_y, M_z) \rightarrow (M_x, -M_y, -M_z)$ (180° plane rotation) are needed in spin–echo experiments.

Even though pulses that are based on adiabatic passage principles have limited application, they are still of great value in a variety of NMR experiments, including those that require spin excitation, T_1 measurement, and multidimensional localization. Furthermore, because of their relative simplicity they are suitable for demonstrating some of the adiabatic principles, as shown in the next section.

Modulation Functions of Adiabatic Passage Pulses

The choice of modulation function will determine to what extent the adiabatic condition is satisfied and thereby the $\mathbf{B}_1$ range over which the pulse executes the desired rotation. For example, an AHP excitation pulse can be executed with sine/cosine modulation functions (*16*) (following convention, the adiabatic pulses are specified according to the modulation functions for $f_B(t)$ and $f_\omega(t)$, respectively), according to

$$\mathbf{B}_1(t) = \mathrm{B}_{1\,\max}\sin\left(\frac{\pi t}{2T}\right)[\boldsymbol{x}'] \qquad [11]$$

$$\left(\frac{\Delta\boldsymbol{\omega}(t)}{\gamma}\right) = \left(\frac{\Delta\omega_{\max}}{\gamma}\right)\cos\left(\frac{\pi t}{2T}\right)[z'] \qquad [12]$$

t varies from 0 to T, and T is the duration of the AHP pulse. The same modulation function can be used for AFP inversion simply by varying t from 0 to $2T$. For these modulation functions, the adiabatic condition can be calculated with Eq. [5] and is given by Eq. [13]:

$$\left|\gamma\mathbf{B}_e(t)(\mathrm{d}\alpha(t)/\mathrm{d}t)^{-1}\right| = (4\Delta\omega_{\max}T/2\pi)\upsilon^{-1} \times\left[\cos^2\left(\frac{\pi t}{2T}\right) + \upsilon^2\sin^2\left(\frac{\pi t}{2T}\right)\right]^{3/2} \qquad [13]$$

where $\upsilon = \gamma\mathrm{B}_{1\,\max}/\Delta\omega_{\max}$. From Eq. [13] it can be seen that, for the on-resonance case, the adiabatic condition—and with it the adiabaticity of the pulse—can be described by two parameters, υ and $\Delta\omega_{\max}T$. Equation [13] can be rewritten in many forms and hence several combinations of parameters can be used to describe the adiabatic condition; in this article we use υ and $\Delta\omega_{\max}T$.

The adiabatic condition is satisfied and the desired rotation is executed when $|\gamma\mathbf{B}_e(t)(\mathrm{d}\alpha(t)/\mathrm{d}t)^{-1}| \gg 1$ over the duration of the pulse. So by evaluating Eq. [13], qualitative information about the $\mathbf{B}_1$ range over which the pulse works according to adiabatic principles can be obtained (*14*). Quantitative information about the adiabaticity of AHP pulses can be obtained by numerical integration of the Bloch equations, typical results of which are shown in Fig. 5. Calculations were performed for the sin–cos-modulated AHP pulse described by Eqs. [11] and [12] and for a tanh-tan-modulated pulse described by

$$\mathbf{B}_1(t) = \mathrm{B}_{1\,\max}\tanh\left[\frac{\zeta t}{T}\right][\boldsymbol{x}'] \qquad [14]$$

$$\left(\frac{\Delta\boldsymbol{\omega}(t)}{\gamma}\right) = \left(\frac{\Delta\omega_{\max}}{\gamma}\right)\frac{\tan\left[\kappa\left(1-\frac{t}{T}\right)\right]}{\tan[\kappa]}[z'] \qquad [15]$$

The constants ζ and κ are set to 10 and arctan[20], respectively (*13*). One also can calculate a sech–tanh-modulated pulse, which defines the hy-

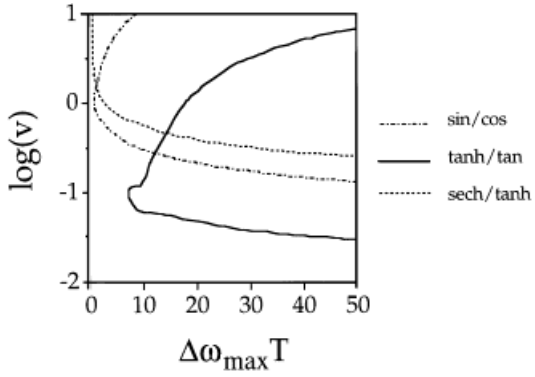

Figure 5 The operational $\gamma B_{1\,max}/\Delta\omega_{max}$ ($\log(\upsilon)$) range versus $\Delta\omega_{max}T$ of an AHP pulse with $\mathbf{B}_1(t)$ and $\Delta\omega(t)$ modulations given by sin–cos (----), tanh–tan (-·-·-·-) and sech–tanh (——), respectively. The lines show the range at which the transformation $\boldsymbol{M}_z \rightarrow \boldsymbol{M}_{xy}$ is executed for 95%.

perbolic secant pulse of Silver and Hoult (*10*), as described above.

Figure 5 shows the $\Delta\omega_{max}T$ and $\gamma B_{1\,max}/\Delta\omega_{max}(=\upsilon)$ region, where the pulses execute the rotation $\boldsymbol{M}_z \rightarrow \boldsymbol{M}_x$ with $\geq 95\%$ efficiency. Figure 5 clearly illustrates that the particular modulation functions used have strong effects on the performance of the pulse. The sech–tanh-based pulse works at lower $\Delta\omega_{max}T$ values (which is in general favorable when slice selection is required), but needs higher $\gamma B_{1\,max}/\Delta\omega_{max}$ to start working. The tanh–tan pulse works at lower $\gamma B_{1\,max}/\Delta\omega_{max}$ values, but has a relatively low upper $\gamma B_{1\,max}/\Delta\omega_{max}$ limit (nevertheless, the range of $\mathbf{B}_1$ insensitivity is still >100) and operates only with higher $\Delta\omega_{max}T$ values. (This is favorable when a large spectral width needs homogeneous excitation.) The sin–cos-based pulse has intermediate characteristics.

By evaluating the adiabatic condition, it is in principle possible to construct optimized modulation functions that work over predetermined ranges for υ and $\Delta\omega_{max}T$. The adiabatic condition can be written with two commonly used modulation functions (sech–tanh, sin–cos), driven with an arbitrary function of time $\eta(t)$ (e.g., $\sin(\eta(t))/\cos(\eta(t))$). By numerically evaluating the constructed adiabatic condition over a predetermined υ and $\Delta\omega_{max}T$ range, $\eta(t)$ can be calculated such that the $\eta(t)$-modulated functions satisfy the adiabatic condition over the predetermined range during the entire pulse length. Detailed discussions of this NOM (numerically optimized modulation) procedure are found in Refs. 17 and 18.

The initial choice of modulation functions for the NOM procedure is not important as long as the functions satisfy boundary conditions. This is because, in the NOM procedure, the optimized modulation functions are calculated to compensate for the deficiencies of the initial functions. The calculated NOM functions are in several ways superior to the initial functions: The range of $\mathbf{B}_1$ insensitivity of the pulses can be predetermined, they can operate over a larger $\mathbf{B}_1$ range (up to >100 times variation in $\mathbf{B}_1$), and they can be constructed to achieve $\mathbf{B}_1$ insensitivity at lower peak power. The NOM procedure can easily be extended to incorporate off-resonance behavior (*14*). In addition to parameters υ and $\Delta\omega_{max}T$, a third parameter $\Delta\Omega/\gamma B_{1\,max}$ is needed in that case to describe off-resonance behavior. $\Delta\Omega$ is the frequency offset. After incorporation of this extra parameter in the adiabatic condition, the rest of the NOM procedure is the same as for the on-resonance case, except that the adiabatic condition is now examined over predetermined υ and $\Delta\Omega/\gamma B_{1\,max}$ ranges. An example of the advantages of NOM-constructed adiabatic rf pulses will be given later.

Off-Resonance Performance of Adiabatic Full-Passage Pulses

The AFP pulse has the attractive characteristic that the inversion is frequency selective: When $|\Delta\Omega| < |\Delta\omega_{max}|$, the pulse executes an inversion; for $|\Delta\Omega| > |\Delta\omega_{max}|$, the net flip angle is zero (see Fig. 6). $\Delta\Omega$ is the frequency offset defined as $(\omega_c - \omega_0)$, the difference between the pulse synthesizer frequency ω_c halfway through the pulse and the Larmor frequency ω_0. The principle of frequency-selective inversion can be understood best by considering the general modulation functions, given by Eqs. [7] and [8]. Figure 6 shows the rotation of the effective field $\mathbf{B}_e$ and the magnetization vectors $\boldsymbol{M}_x$, $\boldsymbol{M}_y$, and $\boldsymbol{M}_z$. At the beginning of the pulse, $\mathbf{B}_e$ is given by $\gamma\mathbf{B}_e = (\Delta\Omega + \Delta\omega_{max})[z']$, whereas $\gamma\mathbf{B}_e = (\Delta\Omega - \Delta\omega_{max})[z']$ at the end of the pulse. Thus, $\mathbf{B}_e$ is still inverted at the end of the pulse for $|\Delta\Omega| < |\Delta\omega_{max}|$ as is shown in Figs. 6(A) and 6(B). Because $\boldsymbol{M}_z$ was initially parallel to $\mathbf{B}_e$, it will remain so throughout the pulse and will be inverted at the end of the pulse. $\boldsymbol{M}_x$ and $\boldsymbol{M}_y$ are perpendicular to $\mathbf{B}_e$ and will rotate about $\mathbf{B}_e$ as a function of $\mathbf{B}_1$ and $(\Delta\omega/\gamma)$ through an angle β given by Eq. [6].

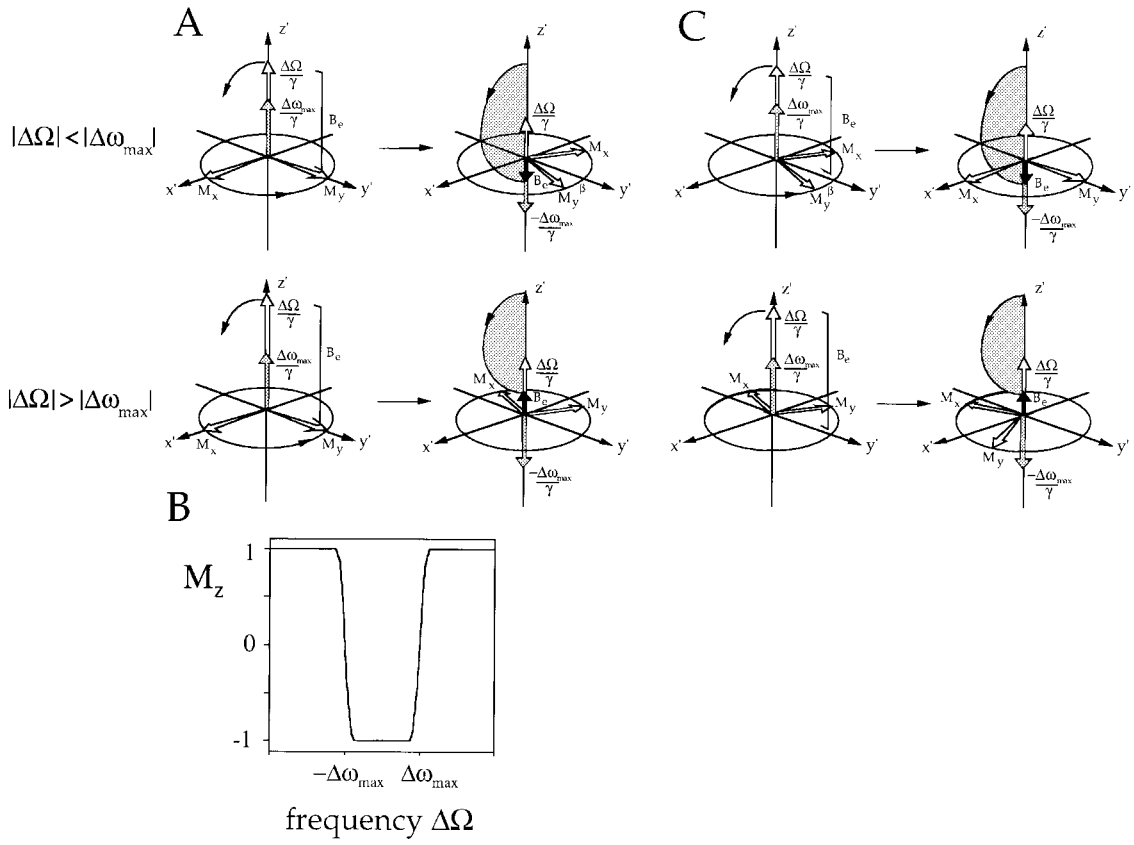

Figure 6 Off-resonance rotations of the effective field $\mathbf{B}_e$ during an AFP pulse and the corresponding rotations of the magnetization vectors $\boldsymbol{M}_x$ and $\boldsymbol{M}_y$. $\boldsymbol{M}_z$ is not drawn because it follows $\mathbf{B}_e$ throughout the pulse. (A) Within the frequency range ($|\Delta\Omega| < |\Delta\omega_{max}|$) $\boldsymbol{M}_z$ inverts and $\boldsymbol{M}_x$ and $\boldsymbol{M}_y$ experience a $\mathbf{B}_1$- and offset-dependent phase shift β. Outside the slice ($|\Delta\Omega| > |\Delta\omega_{max}|$) $\boldsymbol{M}_z$ initially rotates away from z', but ultimately returns to its initial orientation along $+z'$; $\boldsymbol{M}_x$ and $\boldsymbol{M}_y$ are again dephased by β. (B) Typical inversion slice of an AFP pulse executed with sech–tanh modulation—the well-known hyperbolic secant inversion pulse. (C) Off-resonance rotations of $\mathbf{B}_e$ during a second AFP pulse, immediately following the first pulse as shown in (A). Within the slice, $\boldsymbol{M}_z$ inverts again, thereby returning to its original orientation. Because $\mathbf{B}_e$ is inverted between the two pulses, $\boldsymbol{M}_x$ and $\boldsymbol{M}_y$ now rotate through an angle $-\beta$ within the slice, thereby also returning to their initial orientations. Outside the slice, $\mathbf{B}_e$ is not inverted and $\boldsymbol{M}_x$ and $\boldsymbol{M}_y$ will dephase further to a final phase angle of 2β.

However, if $|\Delta\Omega| > |\Delta\omega_{max}|$, $\mathbf{B}_e$ is not inverted but simply rotates away from the z' axis as $\mathbf{B}_1(t)$ increases, and $(\Delta\omega(t)/\gamma)$ decreases and rotates back to $+z'$ at the end of the pulse. $\boldsymbol{M}_x$ and $\boldsymbol{M}_y$ will again dephase as a function of $\mathbf{B}_1$ and $(\boldsymbol{\Delta\omega}/\gamma)$. Therefore, an inversion frequency band is defined because the magnetization, which is initially along z', is inverted for $|\Delta\Omega| < |\Delta\omega_{max}|$ and is returned to its initial orientation for $|\Delta\Omega| > |\Delta\omega_{max}|$ (Fig. 6(B)).

Figure 6 once more illustrates that an AFP pulse cannot be used for refocusing transverse magnetization, because $\boldsymbol{M}_x$ and $\boldsymbol{M}_y$ will be rotated (dephased) as function of $\mathbf{B}_1$ and $(\boldsymbol{\Delta\omega}/\gamma)$. This is demonstrated in Fig. 7. Figures 7(C) and 7(D) show simulations of the slice profile for a 3.2 ms AFP pulse (with $\Delta\omega_{max} = 1562.5$ Hz and maximum $\mathbf{B}_0$ gradient strength $\mathbf{G}_{max} = 30$ mT/m) based on sech–tanh modulation functions. The slice is obtained using the pulse sequence shown in Fig. 7(A) (only one AFP pulse is used for refocusing). As an alternative for showing $\boldsymbol{M}_x$ and $\boldsymbol{M}_y$, a refocusing pulse can be evaluated by calculating the refocused component and the corresponding phase, as is shown in Fig. 7(E). The refocused component I is defined as the

component of transverse magnetization, which is independent of $\mathbf{B}_0$ inhomogeneities and is symmetrical around the refocusing pulse. Mathematically, the refocused component and its corresponding phase are defined as (*8*, *19*)

$$\text{Refocused component } I = (1/2)\left[(f_{xx} - f_{yy})^2 + (f_{xy} + f_{yx})^2\right]^{1/2} \quad [16]$$

$$\text{Phase } \theta = (1/2)\arctan\left(-(f_{xy} + f_{yx})/(f_{xx} - f_{yy})\right) \quad [17]$$

f_{ab} is the fraction of initial $\boldsymbol{M}_a$ ($a = x$ or y) magnetization before the refocusing pulse, which is converted to $\boldsymbol{M}_b$ ($b = x$ or y) magnetization after the pulse. For a perfect refocusing pulse, the refocused component will be 1 (for ($\boldsymbol{M}_x$, $\boldsymbol{M}_y$, $\boldsymbol{M}_z$) $\rightarrow$ ($\boldsymbol{M}_x$, $-\boldsymbol{M}_y$, $-\boldsymbol{M}_z$), $f_{xx} = -f_{yy} = 1$ and $f_{xy} = f_{yx} = 0$). From Figs. 7(C)–7(E) it follows that an AFP pulse can selectively refocus a slice. However, it also can be seen that a nonlinear phase is present across the slice, which is a function of ($\Delta\boldsymbol{\omega}/\gamma$) (Figs. 7[C]–7[E]) and $\mathbf{B}_1$ (not shown). Figure 7(F) shows the experimental verification of these results. Two-dimensional (2D) images (T_R/T_E = 2000/75 ms) were obtained

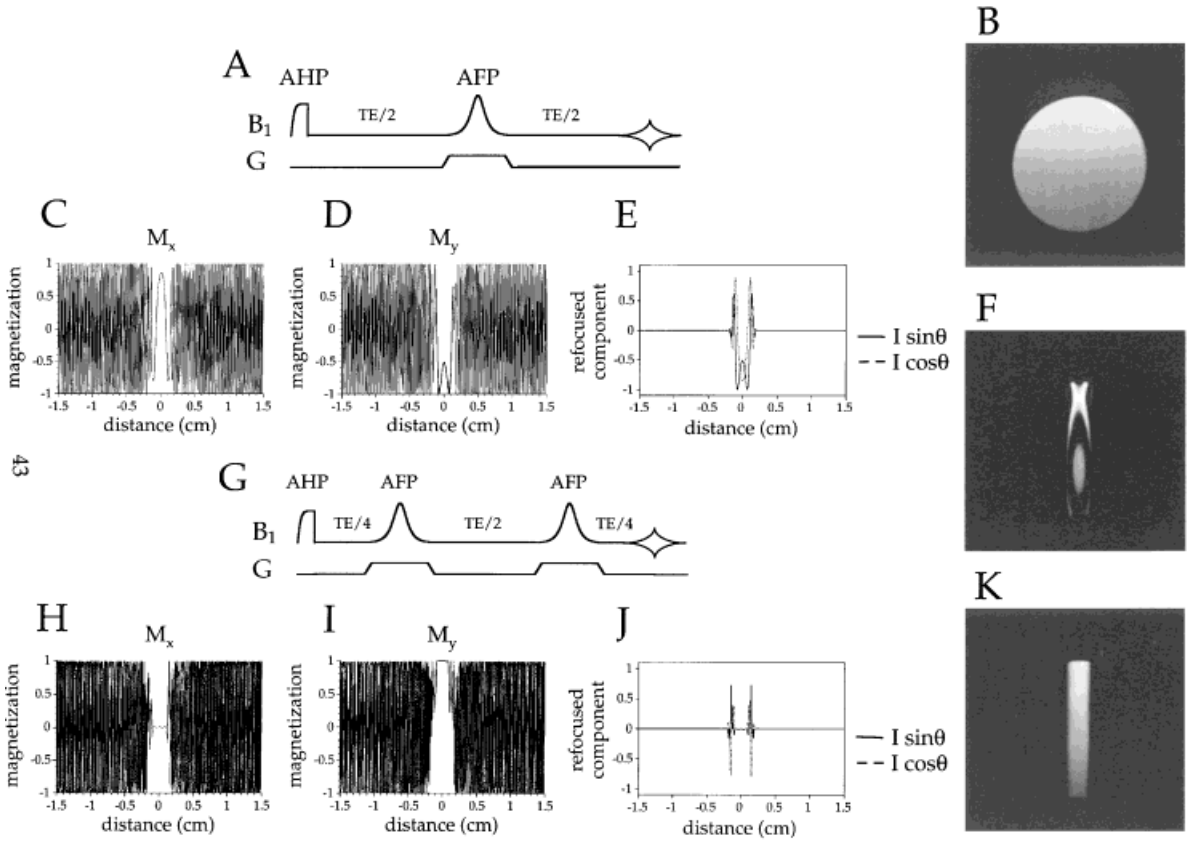

Figure 7 Theoretical and experimental verification of the refocusing capabilities of an AFP pulse. (A) Pulse sequence for obtaining a spatial slice with one AFP pulse. (B) Reference image obtained with a 2.0 cm diameter surface coil of a 1.5 cm diameter spherical phantom containing water. The surface coil is placed on top of the phantom. The image plane is a slice of 2.0 mm thickness. (C)–(E) Simulations of the refocusing capabilities of one 2 ms AFP pulse ($\Delta\omega_{max}$ = 1562.5 Hz, $\mathbf{G}_{max}$ = 30 mT/m) as shown in (A). Simulations show (C) $\boldsymbol{M}_x$, (D) $\boldsymbol{M}_y$, and (E) the refocused component *I*. (F) Image obtained with the pulse sequence as shown in (A) on the phantom as shown in (B). (G) Pulse sequence for obtaining a spatial slice with two AFP pulses. (H)–(J) Simulations of the pulse sequence show in (G), with (H) $\boldsymbol{M}_x$, (I) $\boldsymbol{M}_y$, and (J) the refocused component *I*. (K) Experimental image obtained with the pulse sequence shown in (G). From (H)–(K) it can be concluded that two AFP pulses do generate a useful, well-defined slice without any distortions.

from a 1.5 cm diameter glass sphere with a 2.0 cm diameter surface coil. All images are displayed in a phase-sensitive mode. Fig. 7(B) shows the image (2.5 mm slice thickness) of the sphere without any slice selection in the displayed plane. Fig. 7(F) shows the same image with slice selection in the plane by using one AFP pulse, as shown in Fig. 7(A). These experimental data confirm that one AFP pulse can refocus a slice, but that the slice is indeed strongly degraded by a nonlinear phase and therefore cannot in practice be used.

Application of a second AFP pulse causes the dephasing of M_x and M_y by the first AFP pulse to be rephased for $|\Delta\Omega| < |\Delta\omega_{max}|$, as is shown in Fig. 6(C). For $|\Delta\Omega| < |\Delta\omega_{max}|$, $\mathbf{B}_e$ is inverted and M_x and M_y will experience a total rotation of $\beta - \beta = 0$, where β is again given by Eq. [6] (M_x and M_y return to their initial orientations). For $|\Delta\Omega| > |\Delta\omega_{max}|$, $\mathbf{B}_e$ is not inverted and M_x and M_y will therefore dephase further through an angle $\beta + \beta = 2\beta$. Figures 7(H)–7(J) show simulations for two consecutive AFP pulses as depicted in the pulse sequence of Fig. 7(G). Inside the slice, M_x and M_y indeed return to their initial orientations; outside the slice, the magnetization is dephased twice as much as it is with one AFP pulse (*3, 4*). Because two AFP pulses grouped together as one rf pulse result in a net rotation of 0°, $\mathbf{B}_0$ inhomogeneities and $\mathbf{B}_0$ gradient and off-resonance effects will not be refocused. By placing the two AFP pulses as shown in Fig. 7(G), in analogy with the PRESS localization sequence (*20*), all inhomogeneities will be refocused and a well-defined slice can be obtained without a nonlinear phase roll across the slice (Fig. 7(K)).

Adiabatic Plane Rotation Pulses

As mentioned above, AHP and AFP pulses are not plane rotation pulses, in that they do not rotate all magnetization vectors with arbitrary orientation about the same axis and through the same angle. However, above it was shown that a net refocusing plane rotation pulse can be obtained by executing two AFP pulses: The second AFP pulse rephases the magnetization perpendicular to $\mathbf{B}_e$. From this notion, two general principles in the construction of plane rotation pulses can be deduced. First, in the second rotating frame, the transformation of any magnetization vector must be an identity transformation: The net rotation in the second rotating frame at the end of the pulse must be zero. Second, the desired plane rotation will be achieved by rotating the second rotating frame relative to the frequency frame through the desired angle.

The first principle is satisfied by executing one or more $\mathbf{B}_e$ inversions. This can be seen in the following way. During an AHP or time-reversed AHP, components of $\mathbf{M}$ initially collinear with $\mathbf{B}_e$ remain so throughout the pulse. Similarly, components of $\mathbf{M}$ initially perpendicular to $\mathbf{B}_e$ will remain so, but they also will rotate about $\mathbf{B}_e$ through an angle β given by Eq. [6], or by $\gamma\int \mathbf{M} \times \mathbf{B}_e dt$. If a $\mathbf{B}_e$ inversion is executed, the second part of the pulse will rotate components of $\mathbf{M}$ perpendicular to $\mathbf{B}_e$ through and angle $-\beta$ about $\mathbf{B}_e$ so that the net rotation of $\mathbf{M}$ will be zero at the end of the pulse ($\mathbf{M}$ achieves an identity transformation in the second rotating frame).

$\mathbf{B}_e$ inversions can be achieved by inverting $(\Delta\boldsymbol{\omega}/\gamma)$ halfway through the pulse, when $\mathbf{B}_1 = 0$, or by inverting $\mathbf{B}_1$ (by adding a 180° phase shift) when $(\Delta\boldsymbol{\omega}/\gamma) = 0$. However, for relatively simple adiabatic pulses (*11, 14*) consisting of only two segments, the $\mathbf{B}_e$ inversion can be properly executed only on resonance ($\Delta\Omega = 0$). Off resonance, $\beta = \gamma\int \mathbf{M} \times \mathbf{B}_e dt$ of the second segment can no longer completely compensate β induced by the first segment. Hence, $\mathbf{M}$ no longer executes an identity transformation in the second rotating frame.

More complicated pulses, such as the plane rotation pulse BIR-4, do not have this problem for $|\Delta\Omega| < |\Delta\omega_{max}|$.

Variable-Angle Adiabatic Plane Rotation Pulse

The BIR-4 ($\mathbf{B}_1$-insensitive rotation) pulse (*13, 21*) is composed of four segments (Fig. 8) each of which is an AHP pulse (segments 2 and 4) or time-reversed AHP pulse (segments 1 and 3). The $\mathbf{B}_1(t)$ and $\Delta\boldsymbol{\omega}(t)$ modulation functions shown are given by Eqs. [14] and [15] for an AHP segment. Although BIR-4 can be executed with many modulation functions, this particular pair closely approximates a numerically optimized set of functions derived by the NOM procedure (*12, 18*). The frequency modulation $\Delta\boldsymbol{\omega}(t)$ can be replaced by the equivalent phase modulation $\phi(t)$, which is calculated as the time integral of $\Delta\boldsymbol{\omega}(t)$ according to Eq. [9] (Fig. 8).

The flip angle generated by BIR-4 is determined by the values of two discontinuous phase shifts, $\Delta\phi_1$ and $\Delta\phi_2$, which occur between the first and second segments and between the third and fourth segments of the pulse. To induce an

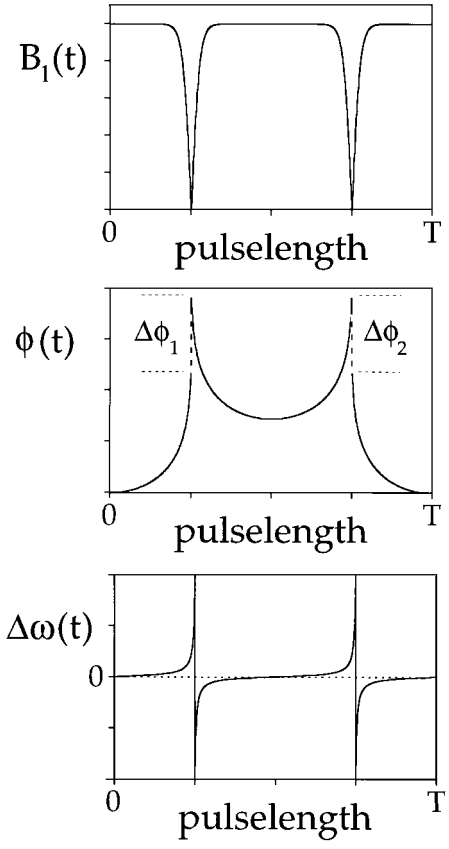

Figure 8 rf amplitude ($\mathbf{B}_1$), phase (ϕ), and frequency ($\Delta\omega$) modulation functions of BIR-4. These specific functions (tanh–tan) closely resemble optimized functions obtained with the NOM procedure (*15*).

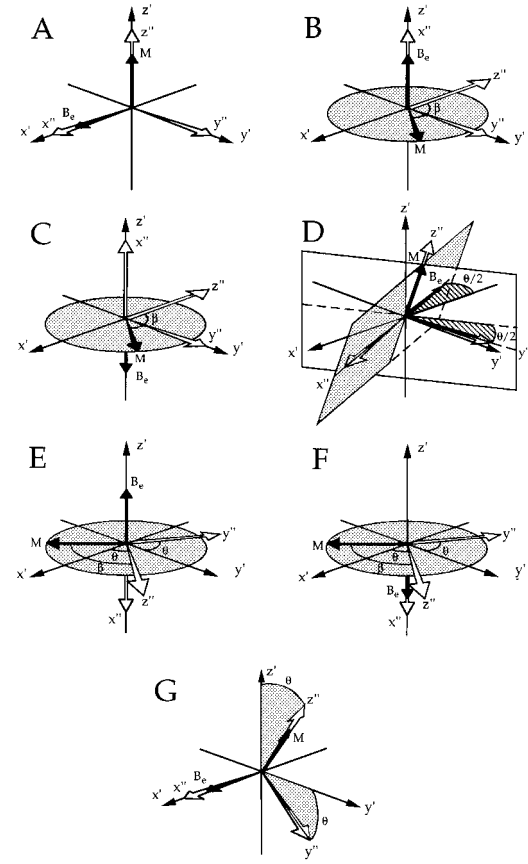

Figure 9 Rotations of the thermal equilibrium magnetization vector in the frequency frame $x'y'z'$ and the second rotating frame $x''y''z''$ during a BIR-4 pulse. Vector representations depict the situation (A) at the onset of the pulse, (B) at the end of the first segment, and (C) at the beginning of the second segment, after the first $\mathbf{B}_e$ inversion and $\mathbf{B}_1$ phase shift. (D) The situation in the middle of BIR-4. In (E) and (F) the situation at the end of the third segment and at the beginning of the fourth segment (after the second $\mathbf{B}_e$ inversion and $\mathbf{B}_1$ phase shift) are shown, respectively. (G) The net rotation in $x''y''z''$ is zero at the end of the pulse. The two discontinuous phase shifts, $\Delta\phi_1$ and $\Delta\phi_2$, cause a net rotation of $x'y'z'$ relative to $x''y''z''$ by an angle θ. (Reprinted with permission from Ref. 6.)

arbitrary flip angle θ, the discontinuous phase shifts are $\Delta\phi_1 = 180° + \theta/2$ and $\Delta\phi_2 = -(180° + \theta/2) = -\Delta\phi_1$.

Figure 9 shows the rotations during BIR-4 in the second rotating frame and of the second rotating frame relative to the frequency frame. Although Fig. 9 shows the rotations only for one magnetization vector (the thermal equilibrium magnetization vector), these rotations are valid for any **M** perpendicular to $\mathbf{B}_e(0)$. Vectors parallel to $\mathbf{B}_e(0)$ are not considered because they remain parallel to $\mathbf{B}_e(t)$ throughout the pulse.

At the onset of BIR-4, $\mathbf{B}_e$ is along x' (and x'') and **M** is along z' (which is collinear with z'') (Fig. 9(A)). The first segment of BIR-4 rotates **M** about $\mathbf{B}_e(t)$ over an angle β away from z''. At the same time, $\mathbf{B}_e(t)$ and the $x''y''z''$ frame are rotated about y'' by 90° (Fig. 9[B]). Between the first and second segments, $\mathbf{B}_e(t)$ is inverted from $+z'$ to $-z'$ and $\mathbf{B}_1(t)$ is simultaneously phase shifted by an angle $\Delta\phi_1 = 180° + \theta/2$ (Fig. 9[C]). During the second segment, **M** is rotated back to z''. At the end of the second segment, z'' (and consequently **M**) makes an angle $\theta/2$ with z', because of the $\Delta\phi_1$ phase shift (Fig. 9[D]). In the third segment, $\mathbf{B}_e(t)$ is rotated rom the $x'y'$ plane to z', thereby causing z'' to make an angle θ with x'. At the same time, **M** is rotated over an angle β away from z'' (Fig. 9[E]). Between the third and fourth segments, $\mathbf{B}_e(t)$ is inverted again from $+z'$ to $-z'$ (Fig. 9[E]) and $\mathbf{B}_1(t)$ is phase shifted by an angle $\Delta\phi_2 = -(180° + \theta/2) = -\Delta\phi_1$. In the final segment, $\mathbf{B}_e(t)$ is rotated to x' and **M** is

rotated to z''. Because z'' makes an angle θ with x' at the end of the third segment, **M** now also makes an angle θ with z' (Fig.9(G)). Figure 9 clearly demonstrates the two general principles underlying the design of adiabatic plane rotation pulses: identity transformation in the second rotating frame and the generation of flip angle θ by rotating the second rotating frame relative to the frequency frame. At the end of BIR-4, the magnetization in the second rotating frame has experienced an identity transformation (the spins have experienced a spin–echo in the second rotating frame), and the actual flip angle is generated by the transformation of the second rotating frame relative to the frequency frame. Although Fig. 9 shows only the on-resonance generation of a flip angle θ by BIR-4, the principles hold for off-resonance magnetization vectors ($\Delta\Omega \neq 0$), provided that $|\Delta\Omega| < |\Delta\omega_{max}|$. For the on-resonance case, the β values generated by the four individual segments are equal in magnitude and their absolute sum is zero ($\beta_1 - \beta_2 - \beta_3 + \beta_4 = 0$). When an inversion of $\mathbf{B}_e$ occurs, the sign of β in the segments that follow also is inverted and does not change until $\mathbf{B}_e$ is inverted again. For the off-resonance case, the magnitudes of β are different in all four segments, because $(\Delta\boldsymbol{\omega}(t)/\gamma)$ is offset by a constant amount. However, their sum is still zero: $\beta_1 = -\beta_3$ and $-\beta_2 = \beta_4$. When $|\Delta\Omega| > |\Delta\omega_{max}|$, $\mathbf{B}_e$ cannot be inverted and the magnetization vectors are not refocused.

BIR-4 is an adiabatic plane rotation pulse that can generate any arbitrary flip angle despite large $\mathbf{B}_1$ inhomogeneities. When compared with AHP pulses, the time symmetry of BIR-4 provides a superior tolerance to off-resonance effects and $\mathbf{B}_1$ inhomogeneities (*13*). (This is analogous to the improved performance of composite pulses relative to a simple square pulse.)

Derivatives of BIR-4

The unique property of BIR-4 to generate an arbitrary flip angle by the introduction of discrete phase jumps within the pulse opens the way to useful derivatives of BIR-4. It was stated earlier than an adiabatic pulse can execute a plane rotation only when the net rotation is zero in the second rotation frame $x''y''z''$. The flip angle is generated by rotating the second rotating frame relative to the frequency frame through the desired angle. However, another way to generate an arbitrary flip angle is to introduce a frequency-dependent phase shift by means of a delay within the pulse. Consider a 0° BIR-4 pulse, $\Delta\phi_1 = -\Delta\phi_2 = 180°$. The net rotation in the second rotating frame is zero, as for all BIR-4 pulses, as long as $|\Delta\Omega| < |\Delta\omega_{max}|$, and the flip angle is zero. A frequency-dependent phase shift can be generated by introducing a delay τ in between the first and second segment of BIR-4 (or, alternatively, between the third and fourth segments), when the magnetization is excited onto the transverse plane. On resonance ($\Delta\Omega = 0$), the delay does not lead to any additional rotation and the final flip angle is zero. However, off-resonance ($\Delta\Omega \neq 0$), the magnetization will rotate through an angle $2\pi\Delta\Omega\tau$. At the end of the delay, BIR-4 is executed further, refocusing all rotations except for the additional phase shift $2\pi\Delta\Omega\tau$, leading to a final flip angle of $\sin(2\pi\Delta\Omega\tau)$. This modified BIR-4 pulse is called SSAP (solvent suppression adiabatic pulse) (*22, 23*) and is very useful for water suppression (*23*) or when frequency-selective excitation is required —for example for spectral editing techniques or for the measurement of T_2 relaxation times for coupled spins (*6*). SSAP can, for instance, also be used for selective water–fat imaging, which can provide relevant information on the composition of a variety of tissues. Figure 10(A) shows a 2D image ($T_R = 2.5$ sec, and $T_E = 25$ ms) obtained with a spin–echo sequence and a 2.0 cm diameter surface coil using a 2 ms 90° BIR-4 for excitation and a pair of 2 ms AFP pulses for slice-selective (2.5 mm slice thickness) refocusing. The object under investigation was a 1.5 cm diameter sphere containing water in a 2.5 cm diameter cylinder containing fat. Fig. 10(A) shows the water and fat compartments; the chemical shift artifact is clearly visible as a spatial displacement of the fat compartment. Figures 10(B) and 10(C) are water and fat images, respectively, obtained with the same sequence, except that the 90° BIR-4 excitation pulse was replaced with a 2 ms SSAP pulse. In Figs. 10(B) and 10(C) the offset of SSAP was set on the fat and water resonances, respectively, and the intrapulse delay τ was set to completely excite the other resonance ($\tau = 1/(4(\Delta\Omega_{water} - \Delta\Omega_{fat}))$). The suppression of the unwanted resonance is complete and insensitive to $\mathbf{B}_1$ inhomogeneities. SSAP is essentially the adiabatic analogue of the well-known jump–return pulse ($90°_{+x}$–τ–$90°_{-x}$). This analogy has been extended to the $22.5°_{+x}$–τ–$45°_{-x}$–

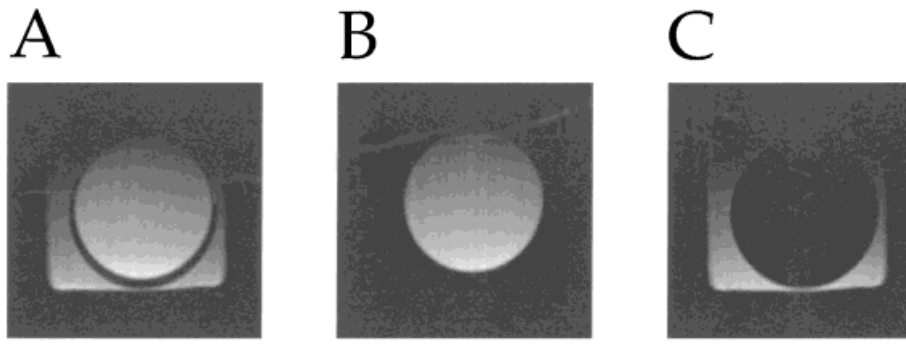

Figure 10 Water–fat imaging using (A) BIR-4 or (B), (C) SSAP for excitation. Slice selection refocusing is achieved with two AFP pulses (see Fig. 7[G]). The phantom consists of a water-filled sphere inserted in a cylinder containing fat. A single surface coil positioned at the bottom of the cylinder was used for rf transmission and reception. (A) Nonselective excitation with BIR-4 leads to the observation of both compartments. Frequency-selective excitation of the water or fat resonances with SSAP leads to the selective observation of (B) water and (C) fat compartments, respectively.

$\tau-22.5°_{+x}$ pulse sequence, under the acronym BIRIANI (*24*).

The features of BIR-4 can be exploited further by introducing two identical delays between the first and second and the third and fourth segments of a 0° BIR-4. Although this does not in general lead to excitation of magnetization, it can distinguish between coupled and uncoupled spins, because a segmented BIR-4 in this form can be seen as a $90°_{+x}-t-180°_{-x}-t-90°_{+x}$ sequence, which is standard for exciting coupled spins: $\mathbf{B}_0$ inhomogeneities and frequency offsets are refocused, but J evolution of coupled spins is not, leading to the excitation of MQCs when a proper evolution period t is chosen ($t \sim 1/4J$, where J is the coupling constant). Uncoupled spins simply experience a 0° BIR-4 pulse and return to their initial orientation. This segmented BIR-4 pulse (and modifications thereof) has been used for homo- and heteronuclear spectral editing (*6, 25–28*).

APPLICATIONS

Several examples demonstrate the versatility of adiabatic pulses for *in vivo* NMR and high-resolution, liquid state NMR measurements. These include fast T_1 measurements of ^{31}P metabolites with BIR-4, improved inversion bandwidths of NOM adiabatic rf pulses, and the use of adiabatic refocusing pulses in multiple-echo spin–echo imaging.

Fast Measurement of T_1 Using BIR-4

Knowledge of T_1 relaxation time is often required for the quantitation of metabolite concentration and for studying exchange mechanisms. Among the most frequently used methods is the inversion–recovery experiment, consisting of an inversion pulse, followed by a variable delay, and an excitation pulse to observe the signal. Although this method gives reliable T_1 it is inefficient: The longitudinal magnetization needs $> 5T_1$ to fully recover to its initial orientation before the next inversion can be executed. This makes the inversion–recovery experiment less desirable for *in vivo* T_1 measurements. Many alternatives for more rapid T_1 data collection have been proposed, including saturation recovery, progressive saturation, and single-scan inversion recovery.

One of the fastest methods is the variable nutation angle (VNA) method (*21, 29–32*), which is easy to implement and gives reliable T_1. In the VNA method, the nutation angle of the excitation pulse is varied, and T_R is short compared with T_1 ($T_R \sim 0.5T_1$) and it is kept constant. This leads to saturation of the signal as function of flip angle, T_R, and T_1. The pulse sequence for the VNA method is shown in Fig. 11(A). The VNA method belongs to a class of steady-state pulse sequences, in which the decrease of longitudinal magnetization due to excitation should equal the increase due to T_1 relaxation. This is accomplished by using "dummy" scans, in which the exact pulse

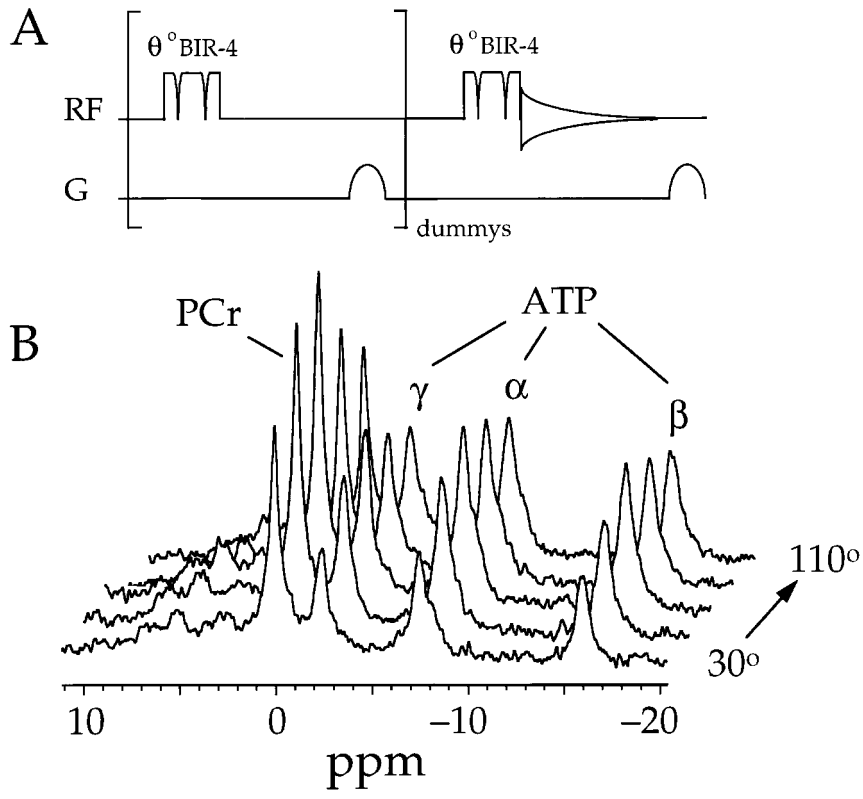

Figure 11 (A) Pulse sequence for the VNA method to measure longitudinal T_1 relaxation time. After several dummy scans (without acquisition) to create a longitudinal steady-state condition, the actual sequence (with acquisition) is executed. The $\mathbf{B}_0$ gradient **G** eliminates unwanted transverse magnetization before excitation. T_1 can be obtained by repeating the experiment with several flip angles θ. The sequence is shown with adiabatic BIR-4 pulses. In the case of square rf pulses, the pulse length is varied to obtain different flip angles. (B) *In vivo* ^{31}P spectra from an intact cat heart obtained with a 18 mm diameter surface coil and the adiabatic VNA method. Flip angles used were 30°, 50°, 70°, 90°, and 110°, respectively, with 64 transients and T_R = 2.5 s. The spectra were analyzed with a frequency-domain-fitting program. The calculated T_1 (using Eq. [18]) for PCr, γ, α, and β-ATP are 2.75, 1.27, 1.37, and 1.38 s, respectively. (Courtesy of C.J.A. van Echteld, Heart-Lung-Institute, Utrecht University Hospital, Utrecht.)

sequence is executed except for acquisition of the signal. Once the longitudinal magnetization is in a steady state, the actual pulse sequence is performed. It can be shown (*30*) that the transverse steady-state magnetization immediately after excitation for a given T_R, T_1, and flip angle θ is given by

$$M_{xy}(\theta) = \frac{\mathbf{M}_0(1 - e^{-T_R/T_1})\sin\theta}{(1 - \cos\theta\, e^{-T_R/T_1})} \qquad [18]$$

$\mathbf{M}_0$ is thermal equilibrium magnetization. Equation [18] is valid only if there is no transverse magnetization before the excitation pulse. This is accomplished by using a homogeneity $\mathbf{B}_0$ gradient spoiler after acquisition. Although the VNA method is fast, it is reliable only if the flip angles are known accurately. With a homogeneous rf coil, this generally is no problem. However, because square rf pulses generate a range of flip angles when an inhomogeneous rf coil (such as a surface coil) is used, the VNA method is unreliable when it is executed with square rf pulses. The unique characteristic of BIR-4 is that it achieves an arbitrary flip angle independent of the $\mathbf{B}_1$ amplitude, making it suitable for the VNA method.

T_1 was obtained on a sphere containing doped water with BIR-4 and square rf pulses, respectively, using a 2.0 cm diameter surface coil for transmission and reception. Inversion–recovery experiments were performed to verify the T_1 data.

Inversion–recovery and VNA experiments were performed with eight delays and flip angles, respectively. The experiments performed with adiabatic pulses yield the same T_1 of 1.34 s. Because of the strong flip angle dependence of the VNA method, the T_1 obtained with square pulses is substantially lower (0.84 s) and unacceptable for use in further calculations. The flip angle dependence of the inversion–recovery experiment is much lower, but when executed with square pulses and a surface coil it nevertheless gives a small error in the obtained T_1 (1.30 s).

Figure 11(B) shows a typical set of ^{31}P spectra obtained with the VNA method and an 18 mm diameter surface coil from an intact cat heart *in vivo*. The flip angles used were 30°, 50°, 70°, 90°, and 110°. The repetition time of 2.5 s for this experiment was dictated by the combined trigger signal of the ventilation rate and cardiac cycle. Each spectrum was the accumulation of 64 transients. After frequency domain fitting of the phosphocreatine (PCr) and ATP resonances, T_1 was calculated using Eq. [18]. The T_1 calculated for PCr, γ, α, and β-ATP was 2.75, 1.27, 1.37, and 1.38 s, respectively.

This example shows that even for relatively simple experiments the advantages of adiabatic pulses over conventional pulses can be substantial. The results are more reliable and S/N is optimized, thereby minimizing experiment time.

Improved Off-Resonance Performance of Adiabatic Inversion Pulses

The most pronounced characteristics of ^{13}C NMR spectroscopy are the very low sensitivity (0.018% of the ^{1}H sensitivity) and the broad chemical shift range of more than 200 ppm. The sensitivity can be increased by using higher $\mathbf{B}_0$ fields. However, this will lead to an increased spectral bandwidth (200 ppm at 4.7 T ($\omega(^{13}\mathrm{C}) = 50$ MHz) is $\sim$ 10 kHz, amounting to $\sim$ 30 kHz at 14.1 T ($\omega(^{13}\mathrm{C}) = 150$ MHz)). Recently, much attention in high-field ^{13}C NMR spectroscopy has been devoted to the development of rf pulses with improved off-resonance performance, mainly for decoupling (*33–37*). Adiabatic rf pulses are almost ideal in this respect: They prevent signal loss due to flip angle errors and their off-resonance performance can be improved with the NOM procedure.

The most demanding tasks for improved rf pulses in high-field ^{13}C NMR are in decoupling and isotropic mixing sequences. For both applications, 180° inversion (and refocusing) pulses are required, so most of the recent developments concentrate on the AFP pulse executed with sech–tanh modulation functions as described by Silver and Hoult (*10*). This hyperbolic secant achieves a well-defined frequency-selective inversion, independent of the $\mathbf{B}_1$ amplitude, above a minimum $\mathbf{B}_1$ threshold. However, sech–tanh modulation is not optimal in inverting large bandwidths with low peak power. Using the adiabatic condition (Eq. [5]), it is possible to optimize the modulation functions to operate at lower peak power. In general, an adiabatic pulse can be described by its $\mathbf{B}_1(t)$ and $\boldsymbol{\Delta\omega}(t)$ modulation functions:

$$\mathbf{B}_1(t) = \mathrm{B}_{1\,\max} f_B(t)[\boldsymbol{x}'] \qquad [19]$$

$$\boldsymbol{\Delta\omega}(t) = [\Delta\Omega - \Delta\omega_{\max} f_\omega(t)][z'] \qquad [20]$$

With these modulation functions, a general adiabatic condition (expressed as a ratio K) can be derived for any time t during the pulse at any frequency offset $\Delta\Omega$:

$$K(\Delta\Omega, t) = \left|\frac{\gamma \mathbf{B}_e(t)}{(\mathrm{d}\alpha(t)/\mathrm{d}t)}\right| = \left(\frac{\Delta\omega_{\max}^2}{\gamma \mathrm{B}_{1\,\max}}\right) \times \frac{\left(\left(\frac{\gamma \mathrm{B}_{1\,\max}}{\Delta\omega_{\max}} f_B(t)\right)^2 + \left(\frac{\Delta\Omega}{\Delta\omega_{\max}} - f_\omega(t)\right)^2\right)^{3/2}}{\left|\left(\frac{\Delta\Omega}{\Delta\omega_{\max}} - f_\omega(t)\right)\left(\frac{f_B(t)}{\mathrm{d}t}\right) - f_B(t)\left(\frac{f_\omega(t)}{\mathrm{d}t}\right)\right|} \gg 1 \qquad [21]$$

To obtain optimized modulation functions, Eq. [21] can be evaluated with the NOM procedure. However, a simpler method has been proposed to improve the off-resonance behavior of adiabatic pulses (*38*). This method of offset-independent adiabaticity states that the adiabatic condition $K(\Delta\Omega, t)$ must be equally satisfied for all $\Delta\Omega$ inside a given bandwidth ($K(\Delta\Omega, t)$ is constant in $\Delta\Omega$ for $|\Delta\Omega| < |\Delta\omega_{\max}|$). Using this requirement, the adiabatic condition can be calculated during the entire pulse when an isochromat at frequency offset $\Delta\Omega$ is on resonance: $f_\omega(t) = \Delta\Omega/\Delta\omega_{\max}$. At time $t_{\Delta\Omega}$—i.e. when the isochromat at $\Delta\Omega$ is on resonance—the adiabatic condition reduces to

$$K(t_{\Delta\Omega}) = \frac{(\gamma B_{1\,\max} f_B(t_{\Delta\Omega}))^2}{\Delta\omega_{\max}\left(\frac{df_\omega(t_{\Delta\Omega})}{dt}\right)} \gg 1 \quad [22]$$

Modulation functions that satisfy the offset-independent adiabaticity can now be calculated with the equality specified by Eq. [22]:

$$\left(\frac{df_\omega(t_{\Delta\Omega})}{dt}\right) = \frac{(\gamma B_{1\,\max} f_B(t_{\Delta\Omega}))^2}{\Delta\omega_{\max} K(t_{\Delta\Omega})} \quad [23]$$

Essentially, Eq. [23] represents the on-resonance condition (where the adiabatic condition is most difficult to satisfy) for all spins in a given bandwidth.

The modulation functions of the hyperbolic secant pulse satisfy Eq. [23]. However, the modulation functions are not optimal when peak power is considered. In general, rf amplitude modulation functions with a flat profile will perform the desired rotation at the lowest peak power, because the rf power is distributed evenly during the pulse. This feature also followed from the NOM procedure (*18*) and by stretching existing adiabatic pulses (*37*). From the theory of offset-independent adiabaticity, so called sin40 adiabatic pulses were developed. They are described by Eqs. [24] and [25]:

$$\mathbf{B}_1(t) = B_{1\,\max}\left(1 - \sin^n\left(\frac{\pi t}{2T}\right)\right)[x'] \quad [24]$$

$$\Delta\boldsymbol{\omega}(t) = \Delta\omega_{\max} - 2\Delta\omega_{\max}\left(\frac{\int_0^t\left(1-\sin^n\left(\frac{\pi t'}{2T}\right)\right)^2 dt'}{\int_0^T\left(1-\sin^n\left(\frac{\pi t'}{2T}\right)\right)^2 dt'}\right)[z'] \quad [25]$$

where $n = 40$ (although the actual value of n is not critical) and $-T \le t \le +T$. These sin40 pulses have a flat rf amplitude profile with rounded edges, making an offset-independent inversion possible at low peak power. Figures 12(A)–12(C) show simulations based on the Bloch equations. Figs. 12 (A) and 12(B) show inversion profiles of a hyperbolic secant ($\Delta\omega_{\max} = 12.5$ kHz) and a sin40 ($\Delta\omega_{\max} = 50$ kHz), respectively. In both cases $T = 2$ ms and $\gamma\mathbf{B}_{1\,\max} = 6.5$ kHz. For both inversion pulses, $\gamma\mathbf{B}_{1\,\max} = 6.5$ kHz is the minimum rf amplitude required to perform an inversion on resonance. However, the inversion bandwidth of a hyperbolic secant pulse is reduced to approximately 25% of the sin40 inversion bandwidth, because a hyperbolic secant pulse needs approximately twice the peak power of a sin40 pulse. This is in agreement with the fact that the effective bandwidth of adiabatic inversion pulses scales with the square of the rf amplitude, as was also derived during the description of stretching existing adiabatic pulses (*33*). This relationship can be extracted as well from Eq. [23], which states that, for given f_B and f_ω modulation functions, the bandwidth $2\Delta\omega_{\max}$ scales with the square of the rf amplitude $(\gamma\mathbf{B}_{1\,\max})^2$.

For comparison, Fig. 12(C) shows the inversion profile of a square pulse ($T = 77$ μs, $\gamma\mathbf{B}_{1\,\max} = 6.5$ kHz). Figs. 12(D)–12(F) show experimental profiles in analogy with the simulations shown in Figs. 12(A)–12(C), respectively. Experiments were performed with a (homogeneous) solenoidal coil on a spherical phantom containing water. After the inversion pulse, the signal was excited onto the transverse plane with an AHP pulse. Spectra were acquired in 1000 Hz steps in which the transmitter frequency of the AFP pulse ranged from −75 kHz to +75 kHz relative to the water resonance. Figs. 12(D)–12(F) confirm the results obtained by numerical integration of the Bloch equations, as shown in Figs. 12(A)–12(C): The high peak power of a hyperbolic secant pulse limits the achievable inversion bandwidth. Because of (small) $\mathbf{B}_1$ inhomogeneities, the on-resonance inversion with square pulses is incomplete (the $\mathbf{B}_1$-dependence is most pronounced on resonance).

It can be concluded that, in addition to the tolerance to large $\mathbf{B}_1$-inhomogeneities, the off-resonance performance of adiabatic pulses is also superior to that obtained with conventional pulses. The off-resonance properties can be improved further with the NOM procedure or by stretching existing adiabatic pulses. However, the procedure of offset-independent adiabaticity yields optimal pulses without intensive and tedious calculations.

Multiecho Spin – Echo Imaging

In multiecho imaging, a range of echo times is sampled in a single scan, thereby significantly reducing the duration of MRI experiments aimed at spatial quantitation of T_2 relaxation times. In multiecho spin–echo sequences, $90°–[t–180°–t–]_n$, the echoes are generated by refocusing

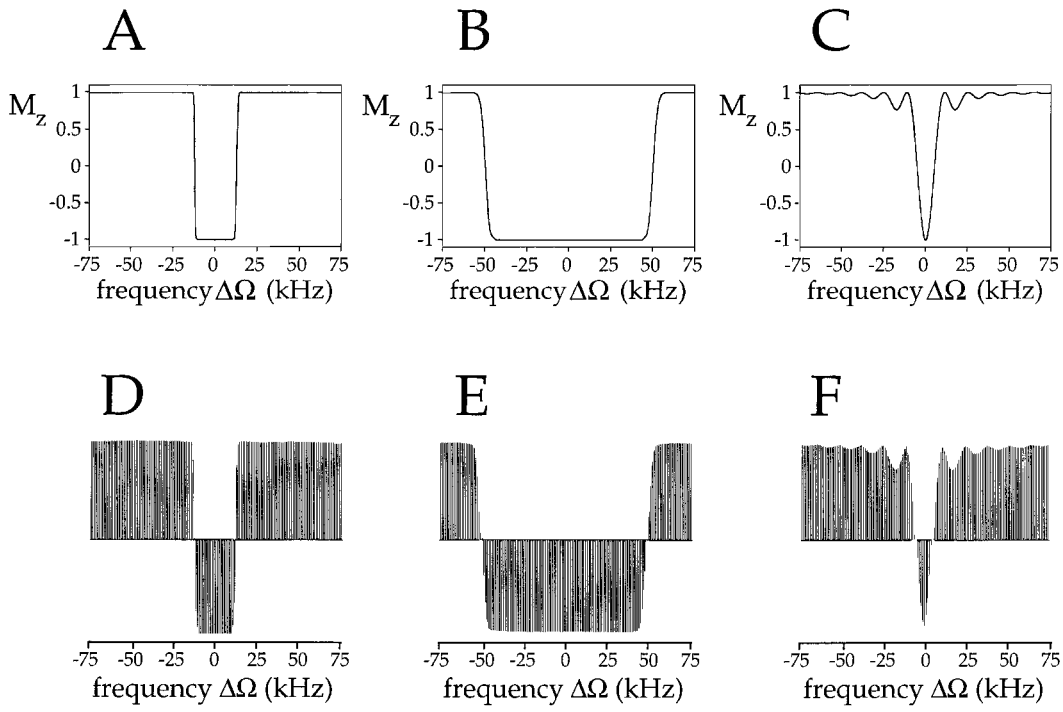

Figure 12 Off-resonance performance of inversion pulses. The inversion profiles of (A) a hyperbolic secant ($\Delta\omega_{max}$ = 12.5 kHz, T = 2 ms), (B) a sin40 ($\Delta\omega_{max}$ = 50 kHz, T = 2 ms), and (C) a square (T = 77 μs) inversion pulse are shown, respectively. In all cases, $\gamma\mathbf{B}_{1\,max}$ = 6.5 kHz, which equals the minimum rf amplitude to perform an inversion on resonance ($\Delta\Omega$ = 0). (D)–(F) The complementary results of experiments using the pulses as indicated in (A)–(C). The experiments were performed with a (homogeneous) solenoidal coil on a spherical phantom containing water. The profiles in (D)–(F) are constructed from 151 spectra covering a total bandwidth of 150 kHz.

pulses. Although this eliminates the effects of $\mathbf{B}_0$ inhomogeneities and frequency offset and minimizes the effects of diffusion, it also makes the experiment more sensitive to flip angle errors. This can lead to an exponentially increasing number of unwanted echoes as more echoes are acquired (*39*). Multiecho spin–echo images will therefore be susceptible to artifacts when they are acquired with a surface coil and conventional rf pulses. Figure 13(A) shows 2D multiecho spin–echo images (data matrix = 256 × 128) of a 6 mm diameter spherical phantom containing water obtained with square rf pulses transmitted with an elliptical surface coil (10 × 15 mm^2). Figure 13(B) shows the same images obtained with adiabatic pulses; 90° BIR-4 for excitation and 180° BIR-4 for refocusing. The images were acquired with T_R = 500 ms and T_E = 11, 63, 114, and 165 ms. No phase cycling or $\mathbf{B}_0$ crusher gradients were applied. The images of the first echo (T_E = 11 ms) are similar in appearance, although the $\mathbf{B}_1$ dependence of square rf pulses leads to a slight reduction in sensitivity, similar to that shown in Fig. 1. In the later echoes, the images obtained with square rf pulses clearly display artifacts (mirror images and strong degradation of the actual image) because of unwanted echoes caused by the $\mathbf{B}_1$-dependence of the rf pulses. Consequently, detailed structural information or quantitative T_2 values cannot be obtained. The adiabatic images do not show an artifact because of the excellent $\mathbf{B}_1$-insensitive refocusing capabilities of BIR-4, which minimize the generation of unwanted echoes. The signal intensity decreases purely because of T_2.

Artifacts in multiecho imaging that result from unwanted echoes can be eliminated by using large $\mathbf{B}_0$ gradient crushers (*39*) or extensive phase cycling. However, neither solution is desirable: $\mathbf{B}_0$ gradient crushers increase the diffusion weighting of the signal and place higher demands on gradient hardware. Extensive phase cycling would lead

to unrealistic measurement times. As shown in Fig. 13, adiabatic rf pulses offer a convenient alternative for eliminating artifacts in multiecho imaging. Adiabatic pulses do not introduce any additional diffusion weighting and do not require any phase cycling, but they do give optimal sensitivity.

RECENT DEVELOPMENTS

Adiabatic pulses in general and BIR-4 in particular offer a wide range of application possibilities. In addition to examples given above, these include multidimensional localization with ISIS (image-selected *in vivo* spectroscopy), with or without OVS (outer volume suppression) (*23, 40*) or with GMAX (gradient modulated adiabatic excitation) (*41*), spectral editing (*6, 26–28*), water suppression (*22–24*), cardiac tagging (*42*), ultrafast imaging (*21*), and spectroscopic imaging (*43*).

With their development in recent years, almost all conventional NMR pulse experiments can be executed with adiabatic pulses. Only the inability of frequency-selective excitation has hampered some applications with adiabatic pulses—for single-shot localization, water suppression without spectral distortions, and multislice imaging, for example. Some of these experiments have nevertheless been executed with adiabatic pulses in an alternative manner. BIR-4 pulses executed with NOM functions generate a well-defined slice profile with strong dephasing of signal outside the slice, in analogy with slice selection and OVS. Because the OVS characteristics of the pulses are nearly perfect, localization is achieved in a single shot with complete immunity to $\mathbf{B}_1$ inhomogeneities. Additional phase cycling of the pulses does not improve the quality of localization, it merely smoothes the slice profile. Therefore, although BIR-4 cannot achieve frequency-selective excitation as can a conventional sinc or gauss pulse, it can be used for three-dimensional spatial localization (*44*).

Two additional selective pulses have been described recently: BISS-8 ($\mathbf{B}_1$-insensitive slice selection using 8 adiabatic segments) (*45*) to achieve single-shot slice selection and BISTRO ($\mathbf{B}_1$-insensitive selective train to obliterate signal) (*46*), which is capable of frequency-selective signal sup-

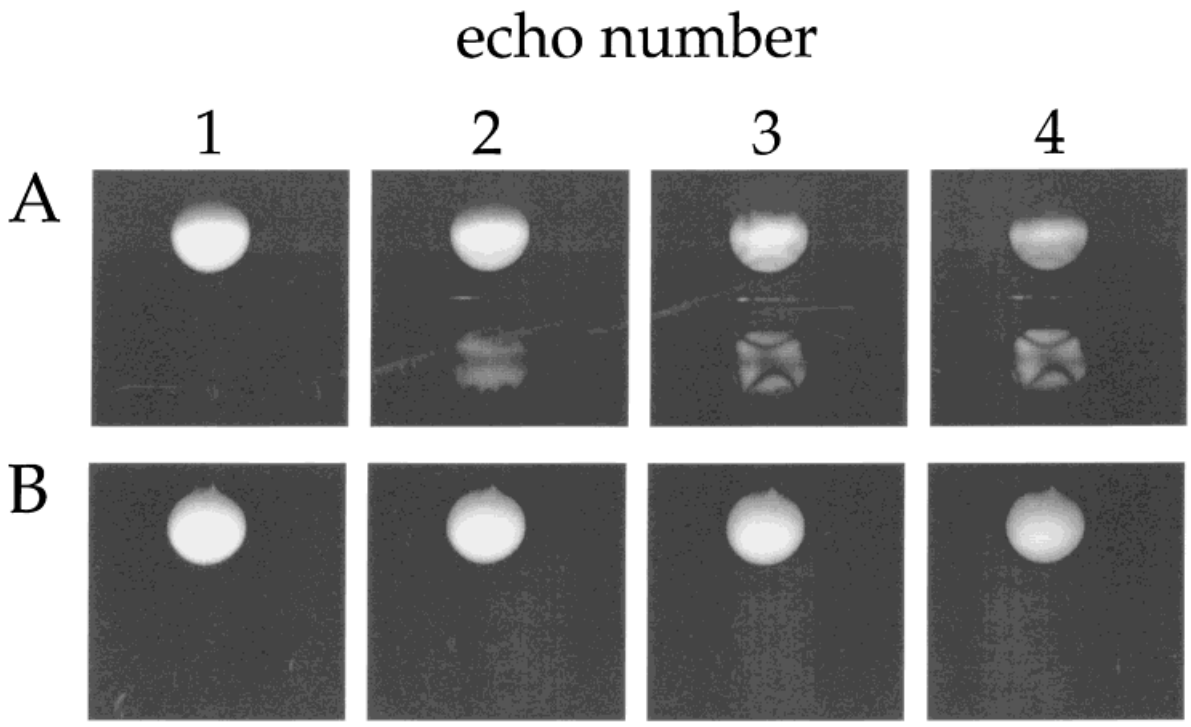

Figure 13 Multiecho spin–echo images of a 6 mm diameter spherical phantom obtained (A) with square pulses and (B) with adiabatic pulses. An elliptical (10×15 mm^2) surface coil was used for rf transmission and reception. Four echoes were acquired at T_E = 11, 63, 114, and 165 ms. No phase cycling or $\mathbf{B}_0$ gradient crushers were applied. (Courtesy of Y. Luo, Abbott Laboratories.)

pression. BISS-8 is an adiabatic pulse that achieves slice selection by executing $\mathbf{B}_1(t)$ and $(\omega(t) - \omega_0)$ modulation in the presence of $\mathbf{B}_0$ gradient modulation $\gamma\mathbf{G}(\mathbf{r}, t)$. By analogy to BIR-4, the flip angle is generated by phase shifts at specific times during the pulse. BISS-8 can be seen as two interleaved BIR-4 pulses, each generating half of the total flip angle. Without $\mathbf{B}_0$ gradient modulation BISS-8 is, just as is BIR-4, not frequency selective. However, because of the $\mathbf{B}_0$ gradient modulation, the total $\Delta\omega(\mathbf{r}, t)$ modulation, which is the sum of $(\omega(t) - \omega_0)$ and $\gamma\mathbf{G}(\mathbf{r}, t)$, is spatially dependent. Within the slice ($|\omega_{max} - \omega_0| > \gamma\mathbf{G}(\mathbf{r})$) the flip angle is determined as if there were no $\mathbf{B}_0$ gradient modulation: $\theta/2 + \theta/2 = \theta$. Outside the slice ($|\omega_{max} - \omega_0| < \gamma\mathbf{G}(\mathbf{r})$), the $\mathbf{B}_0$ gradient modulation inverts $\Delta\omega(t)$ in half of the BISS-8 segments, leading to a flip angle of $-\theta/2$ in those segments and to a total flip angle of $\theta/2 - \theta/2 = 0$.

BISS-8 is the first adiabatic pulse that can achieve slice-selective excitation in a single shot and thus allows multislice imaging, single-shot localization, and OVS with surface coils.

BISTRO is in essence an analogue of the projection presaturation (PP) method of Singh et al. (*47*) Their method consists of several frequency-selective (sinc) rf pulses interleaved with $\mathbf{B}_0$ gradient crushers to eliminate any excited signal. Although PP offers some $\mathbf{B}_1$ insensitivity, the frequency profile deteriorates with increasing rf amplitude. In BISTRO, the sinc pulses are replaced with hyperbolic secant (AFP) pulses. Although they operate adiabatically only when an inversion is executed, the profile stays frequency selective with lower $\mathbf{B}_1$ amplitudes. This also is the main advantage of BISTRO over PP: The frequency profile remains constant irrespective of rf amplitude. Furthermore, the use of an amplitude-modulated envelope function over the AFP pulses significantly increases $\mathbf{B}_1$-insensitivity. BISTRO has been implemented for OVS (*46*) and for water suppression (*44*) with surface coils.

CONCLUSION

With the recent developments of adiabatic rf pulses, it can be stated that almost all experiments executed with conventional rf pulses can now be executed with a high tolerance to $\mathbf{B}_1$ inhomogeneities and other imperfections. This characteristic of adiabatic pulses is valuable in NMR experiments *in vivo*, where surface coils with an extremely inhomogeneous $\mathbf{B}_1$ field often are used for signal enhancement. High-resolution NMR experiments as well can be improved with adiabatic rf pulses, because in general they compensate for all pulse imperfections, including off-resonance effects.

ACKNOWLEDGMENT

We gratefully acknowledge Yanping Luo for contributing Fig. 13, Cees. J. A. van Echteld for contributing Fig. 11, and Michael Garwood for helpful discussions.

REFERENCES

1. D. I. Hoult, R. E. Richards, "The Signal-to-Noise Ratio of the Nuclear Magnetic Resonance Experiment," *J. Magn. Reson.*, **1976**, *24*, 71–85.
2. J. L. Evelhoch, M. G. Crowley, and J.J.H. Ackerman, "Signal-to-Noise Optimization and Observed Volume Localization with Circular Surface Coils," *J. Magn. Reson.*, **1984**, *56*, 110–124.
3. S. Conolly, G. Glover, D. Nishimura, and A. Macovski, "A Reduced Power Selective Adiabatic Spin-Echo Pulse Sequence," *Magn. Reson. Med.*, **1991**, *18*, 28–38.
4. D. G. Schupp, H. Merkle, J. M. Ellerman, Y. Ke, M. Garwood, "Localized Detection of Glioma Glycolysis Using Edited ^{1}H MRS," *Magn. Reson. Med.*, **1993**, *30*, 18–27.
5. L. A. Trimble, J. F. Shen, A. L. Wilman, and P. S. Allen, "Lactate Editing by Means of Selective-Pulse Filtering of Both Zero- and Double-Quantum Coherence Signals," *J. Magn. Reson.*, **1990**, *86*, 191–198.
6. R. A. de Graaf, Y. Luo, M. Terpstra, and M. Garwood, "Spectral Editing with Adiabatic Pulses," *J. Magn. Reson. B*, **1995**, *109*, 184–193.
7. M. R. Bendall, and R. E. Gordon, "Depth and Refocusing Pulses Designed from Multipulse NMR with Surface Coils," *J. Magn. Reson.*, **1983**, *53*, 365–385.
8. M. R. Bendall and D. T. Pegg, "Theoretical Description of Depth Pulse Sequences, On and Off Resonance, Including Improvements and Extensions Thereof," *Magn. Reson. Med.*, **1985**, *2*, 91–113.
9. M. G. Crowley, J. L. Evelhoch, and J.J.H. Ackerman, "The Surface Coil NMR Receiver in the Presence of Homogeneous B_1 Excitation," *J. Magn. Reson.*, **1985**, *64*, 20–31.
10. M. S. Silver, R. I. Joseph, and D. I. Hoult, "Highly Selective $\pi/2$ and π Pulse Generation," *J. Magn. Reson.*, **1984**, *59*, 347–351.

11. K. Ugurbil, M. Garwood, and M. R. Bendall, "Amplitude- and Frequency-Modulated Pulses to Achieve 90° Plane Rotation with Inhomogeneous B_1 Fields," *J. Magn. Reson.*, **1987**, *72*, 177–185.
12. K. Ugurbil, M. Garwood, A. R. Rath, and M. R. Bendall, "Amplitude- and Frequency/Phase-Modulated Refocusing Pulses that Induce Plane Rotations Even in the Presence of Inhomogeneous B_1 Fields," *J. Magn. Reson.*, **1988**, *78*, 472–497.
13. M. Garwood and Y. Ke, "Symmetric Pulses to Induce Arbitrary Flip Angles with Compensation for RF Inhomogeneity and Resonance Offsets," *J. Magn. Reson.*, **1991**, *94*, 511–525.
14. M. Garwood and K. Ugurbil, "B_1 Insensitive Adiabatic RF Pulses" in *NMR Basic Principles and Progress*, Vol. 26, (J. Seelig and M. Rudin, Eds., Springer-Verlag, Berlin, 1992, pp. 109–147.
15. J. Slotboom and W.M.M.J. Bovée, "Adiabatic Slice-Selective rf Pulses and a Single-Shot Adiabatic Localization Pulse Sequence," *Concepts Magn. Reson.*, **1995**, *7*, 193–217.
16. M. R. Bendall and D. T. Pegg, "Uniform Sample Excitation with Surface Coils for *in vivo* Spectroscopy by Adiabatic Rapid Half Passage," *J. Magn. Reson.*, **1986**, *67*, 376–381.
17. G. Town and D. Rosenfeld, "Analytic Solutions to Adiabatic Pulse Modulation Functions Optimized for Inhomogeneous B_1 Fields," *J. Magn. Reson.*, **1990**, *89*, 170–175.
18. K. Ugurbil, M. Garwood, and A. R. Rath, "Optimization of Modulation Functions to Improve Insensitivity of Adiabatic Pulses to Variations in B_1 Magnitude," *J. Magn. Reson.*, **1988**, *80*, 448–469.
19. M. R. Bendall, M. Garwood, K. Ugurbil, and D. T. Pegg, "Adiabatic Refocusing Pulses Which Compensate for Variable rf Power and Off-Resonance Effects," *Magn. Reson. Med.*, **1987**, *4*, 493–499.
20. P. A. Bottomley, "Spatial Localization in NMR Spectroscopy *in vivo*," *Ann. N. Y. Acad. Sci.*, **1987**, *508*, 333–348.
21. R. S. Staewen, A. J. Johnson, B. D. Ross, T. Parrish, H. Merkle, and M. Garwood, "3-D FLASH Imaging Using a Single Surface Coil and a New Adiabatic Pulse, BIR-4," *Invest. Radiol.*, **1990**, *25*, 559–567.
22. B. D. Ross, H. Merkle, K. Hendrich, R. S. Staewen, and M. Garwood, "Spatially Localized *in Vivo* ^{1}H Magnetic Resonance Spectroscopy of an Intracerebral Rate Glioma," *Magn. Reson. Med.*, **1992**, *23*, 96–108.
23. R. A. de Graaf, Y. Luo, M. Terpstra, H. Merkle, and M. Garwood, "A New Localization Method Using an Adiabatic Pulse, BIR-4," *J. Magn. Reson. B*, **1995**, *106*, 245–252.
24. B. A. Inglis, K. D. Sales, and S.C.R. Williams, "BIRIANI: A New Composite Adiabatic Pulse for Water-Suppressed Proton NMR Spectroscopy," *J. Magn. Reson. B*, **1994**, *105*, 61–64.
25. M. Garwood, B. Nease, Y. Ke, R. A. de Graaf, and H. Merkle, "Simultaneous Compensation for B_1 Inhomogeneity and Resonance Offsets by a Multiple-Quantum NMR Sequence Using Adiabatic Pulses," *J. Magn. Reson. A*, **1995**, *112*, 272–274.
26. M. Garwood and H. Merkle, "Heteronuclear Spectral Editing with Adiabatic Pulses," *J. Magn. Reson.*, **1991**, *94*, 180–185.
27. H. Merkle, H. Wei, M. Garwood, and K. Ugurbil, "B_1-Insensitive Heteronuclear Adiabatic Polarization Transfer for Signal Enhancement," *J. Magn. Reson.*, **1992**, *99*, 480–494.
28. S-G. Kim and M. Garwood, "Double DEPT Using Adiabatic Pulses. Indirect Heteronuclear T_1 Measurements with B_1 Insensitivity," *J. Magn. Reson.*, **1992**, *99*, 660–667.
29. K. A. Christensen, D. M. Grant, E. M. Shulman, and C. Walling, "Optimal Determination of Relaxation Times of Fourier Transform Nuclear Magnetic Resonance. Determination of Spin-Lattice Relaxation Times in Chemically Polarized Species," *J. Phys. Chem.*, **1974**, *78*, 1971–1977.
30. R. K. Gupta, "A New Look at the Method of Variable Nutation Angle for the Measurement of Spin-Lattice Relaxation Times Using Fourier Transform NMR," *J. Magn. Reson.*, **1977**, *25*, 231–235.
31. P. A. Bottomley and R. Ouwerkerk, "BIRP, an Improved Implementation of Low-Angle Adiabatic (BIR-4) Excitation Pulses," *J. Magn. Reson. A*, **1993**, *103*, 242–244.
32. H. Sakuma, S. J. Nelson, D. B. Vigneron, J. Hartiala, and C. B. Higgins, "Measurement of T_1 Relaxation Times of Cardiac Phosphate Metabolites using BIR-4 Adiabatic RF Pulses and a Variable Nutation Method," *Magn. Reson. Med.*, **1993**, *29*, 688–691.
33. Z. Starcuk Jr., K. Bartusek, and Z. Starcuk, "Heteronuclear Broadband Spin-Flip Decoupling with Adiabatic Pulses," *J. Magn. Reson. A*, **1994**, *107*, 24–31.
34. M. R. Bendall, "Broadband and Narrowband Spin Decoupling Using Adiabatic Spin Flips," *J. Magn. Reson. A*, **1995**, *112*, 126–129.
35. E. Kupce and R. Freeman, "Adiabatic Pulses for Wideband Inversion and Broadband Decoupling," *J. Magn. Reson. A*, **1995**, *115*, 273–276.
36. M. R. Bendall, "Heteronuclear J Coupling Precession During Spin-Lock and Adiabatic Pulses. Use of Adiabatic Inversion Pulses in High-Resolution NMR," *J. Magn. Reson. A*, **1995**, *116*, 46–58.
37. E. Kupce and R. Freeman, "Stretched Adiabatic Pulses for Broadband Spin Inversion," *J. Magn. Reson. A*, **1995**, *117*, 246–256.
38. A. Tannus and M. Garwood, "Improved Performance of Frequency Swept Pulses Using Offset-Independent Adiabaticity," *J. Magn. Reson. A*, **1996**, *120*, 133–137.
39. A. P. Crawley and R. M. Henkelman, "Errors in T_2 Estimation Using Multislice Multiple-Echo Imaging," *Magn. Reson. Med.*, **1987**, *4*, 34–47.

40. R. J. Ordidge, A. Connelly, and J.A.B. Lohman, "Image-Selected *in Vivo* Spectroscopy (ISIS). A New Technique for Spatially Selective NMR Spectroscopy," *J. Magn. Reson.*, **1986**, *66*, 283–294.
41. A. J. Johnson, M. Garwood, and K. Ugurbil, "Slice Selection with Gradient-Modulated Adiabatic Excitation Despite the Presence of Large B_1 Inhomogeneities," *J. Magn. Reson.*, **1989**, *81*, 653–660.
42. K. Hendrich, Y. Xu, S-G. Kim, and K. Ugurbil, "Surface Coil Cardiac Tagging and ^{31}P Spectroscopic Localization with B_1-Insensitive Adiabatic Pulses," *Magn. Reson. Med.*, **1994**, *31*, 541–545.
43. Y. Luo, R. A. de Graaf, M. Terpstra, H. Merkle, and M. Garwood, "High Resolution (1.5 μl) ^1H CSI of C6 Glioma in Rats," Proceedings of the Second Scientific Meeting, ISMRM, San Francisco, CA, 1994, p. 459.
44. R. A. de Graaf, Y. Luo, M. Garwood, and K. Nicolay, "B_1 Insensitive, Single Shot Localization and Water Suppression," *J. Magn. Reson. B*, **1996**, *113*, 35–45.
45. R. A. de Graaf, K. Nicolay, and M. Garwood, "Single-Shot B_1-Insensitive Slice Selection with a Gradient-Modulated Adiabatic Pulse, BISS-8," *Magn. Reson. Med.*, **1996**, *35*, 652–657.
46. Y. Luo, A. Tannus, and M. Garwood, "Frequency-Selective Elimination of Coherent Signal with B_1 Insensitivity: An Improved Outer-Volume Suppression Method (BISTRO)," Proceedings of the Third Scientific Meeting, ISMRM, Nice, France, 1995, p. 1017.
47. S. Sing. B. K. Rutt, and R. M. Henkelman, "Projection Presaturation: A Fast and Accurate Technique for Multidimensional Spatial Localization," *J. Magn. Reson.*, **1990**, *87*, 567–583.

Robin A. de Graaf studied chemistry at Utrecht University from 1989 to 1993, receiving a M.S. in 1993 for NMR studies of *in vivo* creatine kinase kinetics (supervisor, Klaas Nicolay). In 1994, he worked at the Center for Magnetic Resonance Research, Minneapolis, MN, under the guidance of Michael Garwood on adiabatic pulse design, spatial localization, and spectral editing techniques and their application to an animal tumor model. Currently he is a doctoral student at the Bijvoet Center, Department of *in vivo* NMR, Utrecht University, under the guidance of Klaas Nicolay. His research interests are in adiabatic pulses, spectroscopic imaging, spectral editing, and pulse sequence design.

Klaas Nicolay received a Ph.D. on *in vivo* NMR studies of the metabolism of microorganisms from the University of Groningen in 1983 (thesis supervisor, Robert Kaptein). From 1983 until 1986 he was a postdoctoral fellow of the Netherlands Cancer Research Foundation at Utrecht University (research supervisor, Ben de Kruijff), studying the mechanism of action of anthracycline antitumor drugs with spectroscopic techniques, including NMR. From 1987 to 1991, he was a Huygens Fellow the Netherlands Organization for Scientific Research (NWO) and developed a research program on mitochondrial membrane structure and function. From 1990 to the present, he has been the scientific supervisor of the Netherlands national in vivo NMR facility. He has approximately 70 publications in the field of NMR, and his current research includes the development of *in vivo* NMR techniques for noninvasive studies of tissue metabolism and the regulation of energy metabolism of striated muscle.